PAPER

Check for updates

An effective utilization of MXene and its effect on electromagnetic interference shielding: flexible, free-standing and thermally conductive composite from MXene–PAT–poly(p-aminophenol)–polyaniline co-polymer†

Kanthasamy Raagulan,[a] Ramanaskanda Braveenth,[a] Bo Mi Kim,[b] Kwang Jin Lim,[c] Sang Bok Lee,[d] Miyoung Kim[*c] and Kyu Yun Chai ◍ [*a]

MXene and conductive polymers are attractive candidates for electromagnetic interference shielding (EMI) applications. The MXene–PAT-conductive polymer (CP) composites were fabricated by a cost-effective spray coating technique and characterized using X-ray photoelectron spectroscopy (XPS), scanning electron microscopy (SEM), X-ray diffraction (XRD) and Raman spectroscopy. A new approach has been developed for the synthesis of exfoliated MXene. The MXene–PAT–poly(p-aminophenol)–polyaniline co-polymer composite exhibited good electric conductivity (EC) of 7.813 S cm^{-1}. The composites revealed an excellent thermal properties, which were 0.687 W (m K)$^{-1}$ thermal conductivity, 2.247 J (g K)$^{-1}$ heat capacity, 0.282 mm^2 s^{-1} thermal diffusivity and 1.330 W s$^{1/2}$ m^{-2} K^{-1} thermal effusivity. The composites showed 99.99% shielding efficiency and the MXene–PAT–PANI–PpAP composite (MXPATPA) had EMI shielding effectiveness of 45.18 dB at 8.2 GHz. The reduced form of MXene (r-Ti$_3$C$_2$T$_x$) increased the shielding effectiveness (SE) by 7.26% and the absorption (SE$_A$) was greatly enhanced by the ant farm like structure. The composites possess excellent thermal and EMI SE characteristics, thus can be applied in areas, such as mobile phones, military utensils, heat-emitting electronic devices, automobiles and radars.

[a]*Division of Bio-Nanochemistry, College of Natural Sciences, Wonkwang University, Iksan 570-749, Korea. E-mail: raagulan@live.com; braveenth.czbt@gmail.com; geuyoon@wonkwang.ac.kr; Fax: +82-63-841-4893; Tel: +82-63-850-6230*

[b]*Department of Chemical Engineering, Wonkwang University, Iksan 570-749, Korea. E-mail: 123456@wku.ac.kr*

[c]*Korea Electronics Technology Institute (KETI), Researcher/IT Application Research Center, Korea. E-mail: kjlim@keti.re.kr; miy1kim@keti.re.kr; Tel: +82-63-219-0011*

[d]*Composite Research Division, Korea Institute of Materials Science, Changwon 51508, South Korea. E-mail: leesb@kims.re.kr*

† Electronic supplementary information (ESI) available: Fig. S1: The topology of the composite and MXene under the scanning electron microscope. Fig. S2: The cross-section of the composite under the scanning electron microscope. Fig. S3: XPS O 1s Overlapping curve of composites. Table S1: Elemental percentage of composites from XPS. Table S2: Peak position of elements in composites from XPS. Fig. S4: XPS of FCCNW, CCNW and db-MXene. Fig. S5: XRD of df-MXene, d-MXene, u-MXene, MAX phase, CCNW and FCCNW. Fig. S6: XRD of composites. Table S3: XRD peaks of composites. Fig. S7: Raman spectra comparison of composite in different range. Table S4: Peak position of Raman shift. Fig. S8: (a–g) TGA and DTG analysis of composites (h) thermal diffusivity, thermal conductivity and heat capacity of the composites. Table S5: Thermogravimetric analysis (TG) of the composites, derivative thermogravimetry (DTG) analysis. Table S7: SE of fabricated composites. Table S8: SEA of fabricated composites. Table S9: SER of fabricated composites. Table S10: The bandwidth comparison at about 99.99% shielding efficiency. Table S11: EMI shielding comparison of previous work published and Table S12: The short-listed EMI shielding comparison for graph (Fig. 12e). See DOI: 10.1039/c9ra09522e

1 Introduction

Widespread electromagnetic interference (EMI) is a demanding issue as a consequence of the rapid advancement of miniature electronic components and extensive usage of wireless communication worldwide. The global growth in human population together with the mass production of a variety of electronic devices is creating electromagnetic pollution. EMI is a hot topic, due to the effect on the proximal biological and electronic systems.[1,2] In general, the passage of migrant birds dramatically changes from year to year, due to electromagnetic noise (EMN), which disturbs the natural compass and magnetic positioning capability of migratory birds. Hence, EMN restricts seasonal and natural habitant birds in rural, town, and wild areas.[1–3] Furthermore, EMI also causes various health issues in human, such as headaches, chromosomal mutation, and nervous disorders.[3] When electromagnetic radiation hits a living organism, a dipole environment is created in the body, which creates additional potential, and diminishes the ions transportation through nerves. EMI induces vibration of water molecules, which releases extra heat energy, which is disseminated among organs to generate physiological dysfunction, unhealthy infant, denature of protein, disorder in enzyme function, non-regular function of organelles, and reduction of

fertility, which raise questions about the sustainability of human and other living things on the Earth.[4,5]

EMI shielding is expressed in dB, and is inevitable in the modern electronic world.[3] Non-Ionized Radiation (NIR) has been widely used, as it is safe, even though recent study reports that some NIR radiation has a detrimental issue on biotic structure. The NIR includes extremely low frequency, radio-frequency, microwaves, visible light, and some part of ultraviolet (UV), which can be categorized into perceptible and non-perceptible radiation. The visible region is unharmful, whereas some frequencies of imperceptible radiation potentially have considerable influence on human health. The electron moving materials are the primary source of NIR, while the surrounding environment is a scattering source of NIR.[6–8] Thus, achieving electromagnetic compatibility is indispensable in the current norm. Electromagnetic noise is engendered by various sources, such as thermal background noise, EMI, and terrestrial noise. Diminishing or blocking electromagnetic noise without disturbing adjacent components is considered to be electromagnetic compatibility.[9,10]

To accomplish good electromagnetic compatibility, scientists worldwide utilize numerous strategies by using various materials, such as MXene, metal plate, textile, wax, nonconductive polymer matrix, carbon fabric, intrinsic conductive polymer (ICP), graphite, graphene, carbon nanotube, nanoplate, nanoparticle, plant materials, carbon black, and cement.[11–16] Nonconductive polymers, such as polyvinyl chloride (PVC), nylon,[17] polyvinylidene fluoride (PVDF), polyethylene terephthalate (PET),[18] polydimethylsiloxane (PDMS),[19] polyethylene (PE),[20] polypropylene (PP), polyurethane, and polystyrene[21] are used as supportive matrices for EMI shielding applications. ICPs, such as polyaniline (PANI),[19] polypyrrole (PPy),[22] and polythiophene,[23] are used as a single matrix, or in combination. The combination of different materials is used to create different structural features with enhanced EMI shielding.[17–28] Absorption, reflection, and multiple reflections are central factors for the EMI shielding behaviour of materials, where one aspect of the basic mechanism is more dominant than others. Absorption can be enhanced by increasing the bipolarity of the composite, whereas reflection depends on the electric conductivity of the materials. Absorption happens due to scattering, multiple reflections, and electric and magnetic bipolarity. Nanoparticles possess strong scattering ability, and are able to absorb different energy electromagnetic radiation. Multiple reflections can be enhanced by layered structure and electron flow. The dipolar environment can be created by using polar fillers, and hollow and triangular nanomaterials. Uneven electron distribution in hollow and triangular nanostructure creates polar components that affect EMI shielding.[19–23,29,30]

$Ti_3C_2T_x$/co-doped polyaniline composite exhibits 36 dB of EMI SE with 24.4 S cm^{-1}. The co-doped shows 16 dB of EMI SE and 0.3 S cm^{-1} of EC while pure polyaniline (PANI) exhibits 20 dB of EMI SE and 0.213 S cm^{-1} of EC. In addition, carbon nanotube/polyaniline films displays the EMI shielding of 74.9 dB with 7.5 × 10^4 dB cm^3 g^{-1} of SSE, 3009 S cm^{-1} of EC and thickness of 0.029 mm. The MWCNT/PANI (Ku band), SWCNT/PANI (2–18 GHz), MWCNT/PANI (0.8–3 GHz) composite show 39.2, 31.5, 47 dB of EMI shielding and its corresponding thickness are 2, 2.4

and 0.5 mm, respectively. PEDOT : PSS/waterborne polyurethane (WPU) composite exhibits EMI shielding of 62 dB with 0.15 mm.[24–28] Therefore, increasing thickness of the conductive polymer composites reduces the EMI shielding. Hence, conductive polymer composition should be a thin film.

MXene is a novel kind of two-dimensional ternary metal carbide/nitride derived from the corresponding three-dimensional MAX phase. The MXene possess excellent physical properties such as hydrophilic in nature with good electrical and thermal conductivity, higher specific surface area and excellent film forming ability which are main reason for the preference of MXene than graphene. Hence, MXene and MXene composites become hot topic for EMI shielding application around the world. The various type of MXene have been studied and EMI shielding application mainly focus on $Ti_3C_2T_x$. The Shahzad et al. reported that the $Ti_3C_2T_x$/sodium alginate coating with 45 µm on Polyethylene terephthalate (PET) film shows 92 dB of EMI SE with 4600 S cm^{-1} of electric conductivity.[14,27,28] The ultralight MXene-based aerogels exhibits 75 dB EMI shielding with SSE of 9904 dB g^{-1} cm^3 and density of 0.004 g cm^{-3} where aerogel induced by freeze drying process while MXene Foam exhibits 70 dB of EMI SE with 0.006 cm of thickness 0.22 g cm^{-3} density and SSE of 318 dB g^{-1} cm^3 where foaming induce by hydrazine.[16,24] Moreover, MXene/calcium alginate aerogel exhibits 54.3 dB of EMI shielding with SSE of 40.22 dB g^{-1}. cm^3, thickness 26 µm of and density of 1.35 g cm^{-3}.[25] Hence, introduction of polymers comparatively reduces the EMI shielding of pure MXene, increase the density and give rise various structural features. The graphene/copper nanowire embedded graphene aerogel exhibits 47 dB of EMI SE with 0.2 cm of thickness and EC of 1.208 S cm^{-1}.[26] The MXene polypyrrole (PPy) textile with thickness 1.3 mm (3 times coated) displays EMI SE of 90 dB with 10 S cm^{-1} of EC whereas $Ti_3C_2T_x$/poly(3,4-ethylenedioxythiophene)–poly(styrenesulfonate) (PEDOT : PSS) (7 : 1) with 11.1 µm thickness and 340.5 S cm^{-1} of EC shows 42.1 dB of EMI SE.[12,13] Hence, the MXene is a good choice for EMI shielding compare to the other fillers which is due to the MXene have low density, high electric conductivity, high EMI shielding with micron thickness.

The selective etching strategy has been used to synthesize MXene, for which HF, LiF/HCl, FeF$_3$/HCl, and NH$_4$F/HCl are used. However, the minimally intensive layer delamination (MILD) method uses LiF/HCl, which gives rise to the best quality MXene, compared with other etchants.[31] The general formula of MXene is $M_nX_{n+1}T_x$, while the corresponding MAX phase possesses M_nAX_{n+1} universal symbolization, where M is an early transition metals, A is a group 13/14 element, X is carbon or nitrogen, and T_x is a surface functional group, which include –OH, –F, =O and Cl. During the etching process, the A layer is eradicated, and the corresponding bond between M–A and A–X are substituted by the surface functional groups. Thus, the MXene is formed with the gap between 2 layers. One A layer is a sandwich between two M–X layers, where the M–X bond is stronger than the M–A bond. Hence, depletion of M–A bond is easier than of M–X bond, which remains as MXene.[31–35] So far, many MAX phases and MXenes have been studied, even though Ti_3AlC_2 and its corresponding MXene are widely used for various applications, such as EMI shielding, battery, medical, and capacitors.[31–36]

In this study, we developed a new type of polymer composition called "PAT polymer" solution and a new approached has been made to prepare exfoliated MXene (d-MXene) and reduced MXene (r-MXene). According to our knowledge, this is the first time that the conductive polymers (CP), such as poly(p-aminophenol) (PpAP), polyaniline–PpAP (PANI–PpAP) copolymer were employed for EMI shielding application. We have prepared and analyzed the effectiveness of other CPs, such as polypyrrole (PPy), polyaniline (PANI), polythiophene (PTh) for this study. The general formula of composite was MXPATCP; where MX is MXene, PAT is polymer composition and CP is conductive polymer. Hence, MXPATPN, PXPATPA, MXPATPNPA, MXPATPPy and MXPATPTh composites were successfully fabricated with corresponding conductive polymers, which are PANI, PpAP, PANI–PpAP, PPy and PTh, respectively. The composites without CP are MXPAT, dMXPAT, uMXPAT and rMXPAT which were prepared by using MXene, d-MXene, u-MXene and r-MXene, respectively. The rMXPAT and dMXPAT were used to compare the EMI SE with other composites. The conductive carbon fiber network was denoted as CCNW and functionalized CCNW was denoted as FCCNW. The parameters such as elemental analysis, structural features, thermal stability, thermal conductivity, electric conductivity and EMI shielding were investigated in detail.

2 Materials and method

2.1. Materials

Titanium, Titanium carbide, and aluminium (325 mesh size) were purchased from Materials Korea (Rep. of Korea). Graphene (M-25, average size of 25 μm) was obtained from Ditto Technology (Rep. of Korea). Ethanol (98%), agar, hydrochloric acid (HCl 35%), tetrahydro furan (THF), and aniline were supplied by Samchun (Seoul, Korea). Polyethylene terephthalate (PET) binder (fibre diameter 2.2 dtex, 5 mm) and carbon fibre (fibre diameter 7 μm, 6 mm length) were obtained from TORAY product, (Tokyo, Japan), while polyacrylamide (PAM) was purchased from Sigma Aldrich (Seoul, South Korea). Iron(III) chloride (FeCl$_3$ 97%), lithium fluoride (LiF 300 mesh), pyrrole (98%), thiophene (99%), trimesic acid (98%), 4-aminophenol (98%), acrylic acid, N-methyl-2-pyrrolidone (NMP), and poly-acrylic acid (PAA) were obtained from Sigma Aldrich (Seoul, South Korea). Polyvinyl alcohol (PVA 89%) and polyvinylidene fluoride (PVDF) were supplied by Alfa Aesar (Seoul, Korea). Chitiooligosaccharide (10 000 MW) was provided by Sunchon National University, Biomedical polymer lab, (Jeonju Korea). Glycerin was obtained by reagent from Duksan (Seoul Korea). N,N-Dimethylformamide (DMF) was purchased from Daejung (Seoul Korea). All of the chemicals were used without further purification.

2.2. Synthesis of Ti$_3$AlC$_2$

TiC, Ti, and Al powders with the molar ratio of 2 : 1 : 1 were ball-milled by using Pulverisette 6 Planetary Mono Mill (Fritsch, Germany) in ethanol medium at 200 rpm for 1 h under nitrogen environment, and the resultant mixture was dried at 80 °C for

12 h in vacuum oven. Then, 3 g of the above mixture was cast into disc of 12 mm diameter by applying 27.6 MPa pressure for 5 min in a laboratory press. Subsequently, the disc was treated at 1350 °C with a heating rate of 20 °C min^{-1} in argon environment for 2 h, and cooled to room temperature (RT). The resultant disc was powdered by ball milling in ethanol medium at 300 rpm for 3 h under nitrogen gas. The ethanol was evaporated at 80 °C for 12 h in vacuum oven, and the resultant MAX phase was directly utilized for MXene synthesis.

2.3. MXene (Ti$_3$C$_2$T$_x$) synthesis

First, 1 g of Ti$_3$AlC$_2$ and 1 g of LiF were mixed together in 20 mL of 9 M HCl solution, and stirred at 35 °C for 24 h. The etched product was washed with DI water up to pH 6 by centrifuging at 3500 rpm for 5 min. During the washing process, the colours of the supernatants shown in Fig. 1a and b differ from that of DI water, which is due to the dispersion of MXene flake. The obtained MXene was dehydrated in vacuum oven, until achieving constant weight. The resultant MXene was directly used for the colloidal solution, exfoliated MXene, and composite preparation.

2.3.1. MXene suspension solution and exfoliated MXene (d-Ti$_3$C$_2$T$_x$) preparation. The etched MXene was directly transferred to DI water, and sonicated at (15–17) °C for 1 h under nitrogen environment. The resultant solution was then centrifuged at 3500 rpm for 30 min, and the supernatant was collected and stored at 5 °C for the further process, termed MXene suspension. One portion of MXene suspension was filtered through 0.45 μm nylon membrane filter, and dried at 80 °C in vacuum oven until constant weight was obtained. The concentration of the colloidal solution was calculated as 200 mg L^{-1}, and denoted as df-Ti$_3$C$_2$T$_x$. Another approach that was taken was that the colloidal solution was evaporated at rotavapor at 60 °C, and the volume of colloidal solution reduced. The solution was cooled immediately by pouring cold water onto the evaporating flask, then nitrogen gas was pumped into the rotavapor, until it reached atmospheric pressure. Subsequently, the evaporating flask was removed, and cooled to 5 °C in 30 min. The cold mixture was filtered through 0.45 μm nylon membrane filter, and the solid was dried at 80 °C in vacuum oven, until constant weight was obtained, and denoted as d-Ti$_3$C$_2$T$_x$. This exfoliation process was repeated several
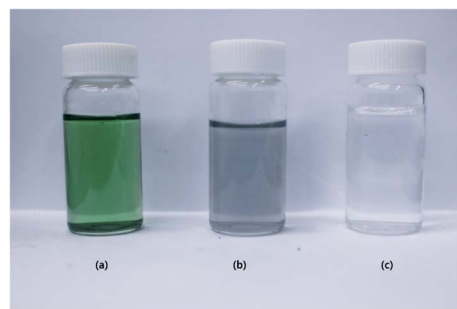

Fig. 1 The supernatant colours of MXene during the washing process (a) 1st centrifuging, (b) final centrifuging, and (c) DI water.

times, until obtaining clear supernatant, and the resultant solid was dark brown in colour, and denoted as u-MXene. Both d-MXene and the u-MXene were collected for further process. The colloidal solution was prepared by using d-MXene by sonicating 30 min in aqueous phase for composite preparation (Scheme 1).

2.4. Conductive polymer (CP) synthesis

2.4.1. Synthesis of polyaniline (PANI). Next, 13.67 mL of aniline was dissolved in 750 mL of 0.2 M HCl, and stirred for 15 min. Then, 0.25 M of ammonium persulfate was added drop-wise into aniline with continuous stirring, and kept 24 h for polymerization, without stirring. The polymer was collected at the filter, and washed thoroughly with an ample amount of 0.2 M HCl, followed by 750 mL of acetone. The product was dried at 60 °C in vacuum oven, and stored at RT for further process.[36]

2.4.2. Synthesis of poly *para*-aminophenol (PpAP). The particular amount of *para*-aminophenol (pAP) (0.2 M) was dissolved in 1000 mL of 0.5 M HCl, and stirred for 15 min; 500 mL of 0.6 M APS was added drop-wise, and stirred for 24 h at RT. Then, the reaction was terminated by adding an amount of methanol. The product was filtered, and washed by 0.5 M HCl, until clear filtrate was obtained, followed by washing with methanol, and then acetone. Each washing was performed until clear filtrate was obtained. The product was then dried at 80 °C for 12 h, and used for further process.[37]

2.4.3. Synthesis of the poly aniline–poly *para*-aminophenol copolymer (PpAP–PANI). Next, 0.1 M of aniline and 0.1 M of pAP were mixed in 1000 mL of 0.5 M HCl, and stirred for 15 min. Then 1000 mL of 0.3 M of APS was added drop-wise, and stirred for 24 h. The yield was filtered, and washed with 0.5 M HCl, methanol, and acetone [S1, S2]. The product was dried at 80 °C in vacuum oven, and stored for further process.[36,37]

2.4.4. Synthesis of poly-pyrrole (pPy). The 0.05 M of pyrrole, 0.1 M FeCl₃, and 0.0225 M of SDS were dissolved and stirred at RT for 4 h. The resultant black colour product was collected at filtration, and washed with a sufficient amount of DI water and ethanol. The collected yield was dried at 40 °C for 12 h in vacuum oven.[38]

2.4.5. Synthesis of poly-thiophene (pTh). Then, 1 g of SDS, 2 g of CTAB, 21 mL of thiophene, and 0.25 g of CuCl₂ were sonicated in 500 mL of DI water for 30 min. The 90 g of APS was dissolved in 500 mL DI water which was added drop-wise into thiophene solution while stirring for 2 h. The resultant mixture was then kept for 24 h, without being disturbed. After that, the yield was washed with ample amount of DI water and ethanol. The product was dried at 50 °C, until constant weight was obtained.[39,40]

2.5. Preparation of conductive carbon fibre network (CCNW) and functionalization

Next, 600 g of carbon fiber, 150 g of PET binder, and 0.3 wt% of dispersant (PAM) were dispersed in a sufficient amount of deionized (DI) water at 500 rpm for 10 min. A drum dryer with 140 °C surface temperature and 7 m min⁻¹ speed was used to produce CCFN. The areal density of the obtained CCFN was 30 g m⁻². The CCNW with 29 cm × 21 cm dimension was dipped into the 2 g L⁻¹ chitiooligosaccharide solution for 2 min, and dried at 100 °C for 12 h. The gained CCNW was denoted as FCCNW, and was used directly for composite preparation.

2.6. Preparation of the PAT solution

The PAT solution was prepared according to Table 1. All the compositions were mixed together, and stirred for 30 min (Fig. 2a), and then the temperature was gradually increased to 130 °C, and the mixture boiled, until it became transparent
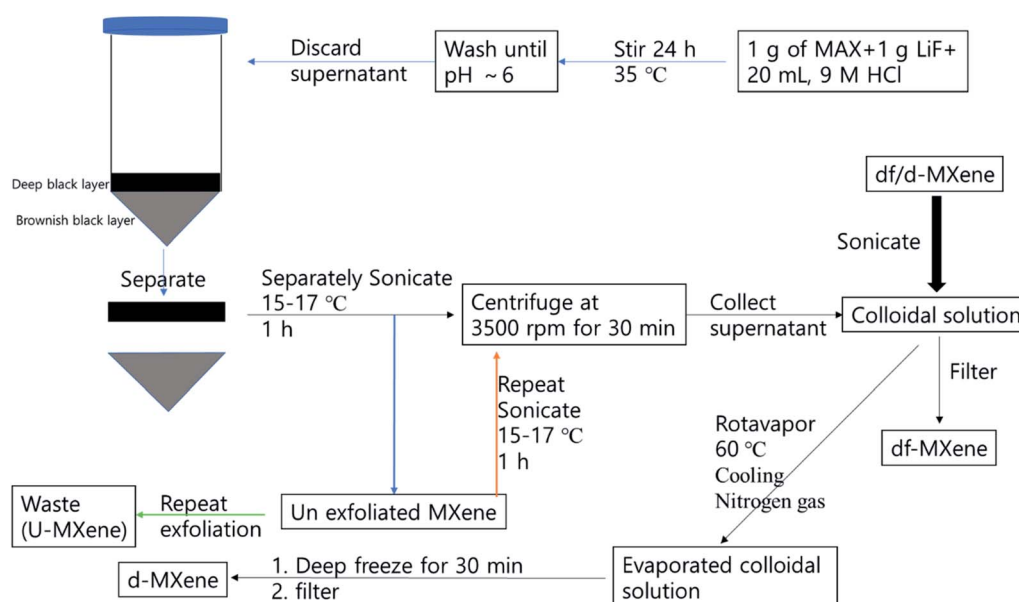
Scheme 1 Flow chart of the synthetic approach of exfoliated MXene synthesis.

Table 1 The composition of the PAT solution

Compounds	Amount for 25 cm^2
Agar	0.397 g
PVA	0.794 g
Trimesic acid	39.675 mg
Acrylic acid	0.198 g
Glycerin	1.984 mL
PVDF in NMP (1 g L^{-1})	1.984 mL
Chitooligosccharide	79.375 mg
Polyacrylic acid	79.375 mg
FeCl$_3$	0.119 g
DI water	35.75 mL

yellow (Fig. 2b). The continuous boiling process gave rise to a transparent brown solution (Fig. 2c), which was obtained as the final composition. The stirring was maintained, until it reached RT. Finally, the volume of the mixture was levelled to the initial volume by adding DI water. The resultant solution was denoted as PAT solution, and used for composition preparation.

2.6.1. Preparation of MXene–PAT polymer composite (MXPAT). The 25 mL of PAT solution and 1.2 g of MXene were stirred together for 24 h, and then the resultant solution was sprayed coated on FCCNW, which was initially dried using an air gun. Next, the dried composite was dehydrated in vacuum oven at 80 °C for 5 h. After that, 50 mL of MXene colloidal solution was sprayed on the composite, and finally, the composite was dried for 1 h in vacuum oven. The final composite was utilized for additional analysis.

2.6.2. Preparation of MXene–PAT-conductive polymer composite (MXPAT-CP). The 10 mL of NMP, 0.795 g of conductive polymer, and 1.2 g of MXene were stirred together for 24 h. The mixture was transferred into 25 mL of PAT solution, and stirred for 1 day. The resultant solution was sprayed coated on FCCNW, which was dried using an air gun, and then dehydrated in vacuum oven at 80 °C for 5 h. The 50 mL of MXene colloidal solution was sprayed on the composite, and dried for 1 h in vacuum oven. The corresponding composite of the polymers of PANI, PpAP, PANI–PpAP, pTh, and pPy were denoted as MXPATPN, PXPATPA, MXPATPNPA, MXPATPTh, and MXPATPPY, respectively. Then the composites were utilized for additional analysis.

2.6.3. Preparation of reduced MXene (r-MXene) and r-MXene–PAT composite (rMXPAT). First, 1 g of LiAlH$_4$ and 5 g of MXene were mixed together in sufficient amount of tetrahydrofuran (THF) solution, and stirred for overnight. Then the resultant mixture was filtered, and washed with ample amount of THF. After that, the product was dried at 80 °C in a vacuum oven for overnight. Next, the 1.2 g of r-MXene was mixed with 25 mL of PAT solution, and stirred for 24 h. The resultant dispersed solution was sprayed on FCCNW, and the composite was then dried at 80 °C in a vacuum oven for 5 h. The surface coating was done by spraying 50 mL of MXene colloidal solution onto the composite, and finally dried for 1 h in vacuum oven. The composite was denoted as rMXPAT.
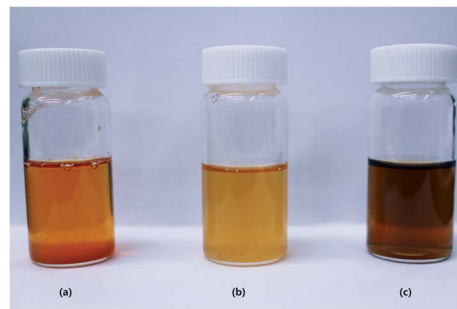

Fig. 2 The liquid PVA–agra polymer composition.

2.7. Characterization

A field emission scanning electron microscope (SEM), S-4800 (Hitachi, Tokyo, Japan) was used to examine the surface morphology and cross-section of the composites. A High-power X-ray Diffractometer D/max-2500V/PC, (Ragaku, Tokyo, Japan) with Cu(Kα) was used to record the X-ray diffraction patterns of the composites. XPS with a (30–400) μm spot size at 100 W of Emax (Al anode) (K-Alpha, Thermo Fisher, East Grinstead, UK) was used to analyze the chemical environment and elemental percentage of the composites. The four-probe method FPP-RS8, DASOL ENG (Seoul, Korea) was used to measure the electric conductivity of the composites. The thermal stability of the composites was tested using a Thermal Analyzer DSC TMA Q400 (TA Instruments Ltd., New Castle, DE, USA). The thermal diffusivity, thermal conductivity, heat capacity and density were measured by using Laser Flash Apparatus LFA 467 (NETZSCH, Wittelsbacherstrabe, Germany). High-resolution Raman spectrophotometry (Jobin Yvon, LabRam HR Evolution (Horiba, Tokyo, Japan)) was utilized to study structural features of the composites. A Mitutoyo thickness 2046S dial gage (Mitutoyo, Kanagawa, Japan) was used to measure the thickness of the composites. The X-band (8.2–12.4) GHz EMI shielding was measured using a vector network analyzer (VNA, Agilent N5230A, Agilent Technologies, Santa Clara, CA, USA) with a sample size of 22.16 mm × 10.16 mm.

3 Results and discussion

3.1. Scanning electron microscope (SEM) analysis

The microstructure of Ti$_3$AlC$_2$ displayed metallic polycrystalline layered structure with higher aspect ratio. In general, MAX phase possesses hexagonal crystal structure with $P6_3/mmc$, where M–X forms an octahedral structure that is sandwiched between A layers. The cross section of the bulk Ti$_3$AlC$_2$ has smooth surface and layers are arranged like crystal rock (Fig. 3a).[13,14,24–27,41,42] The morphology of MXene under SEM showed layers that were separated by gaps created by the etching process where A layers are eradicated. In addition, single layers of MXene were also observed in multilayer stack of MXene, which is due to the complete depletion of A layers. The cross section of MXene with a loosely stacked "accordion" structure indicates the successful occurrence of etching process and some individual flakes are observed on the surface of
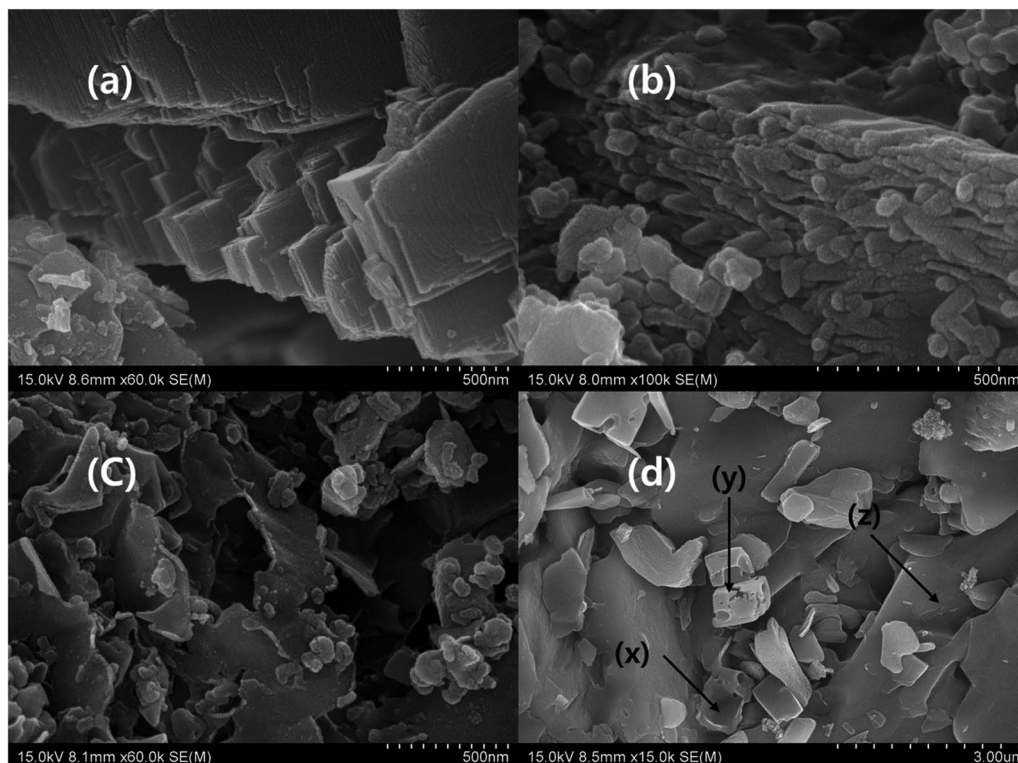
Fig. 3 SEM image of (a) Ti_3AlC_2 ($\times 50\,000$), (b) $Ti_3C_2T_x$ ($\times 100\,000$), (c) d-MXene ($\times 60\,000$), and (d) u-MXene ($\times 15\,000$).

MXene stack which confirms the complete separation of MXene layers from the stack (Fig. 3a, b and Scheme 1). The cross section of pure MXene film reveals that the edge curling is common and exfoliated MXene can join together and form MXene film which is mainly due to the hydrogen bond.[14,24–27,41–43] The exfoliation process separates the layers of MXene stack, and forms single layers of MXene (Fig. 3c). The curling of the brink of single-layer MXene showed irregular shape, and the size also varied, even though a few small sized flakes which formed due to the curling, were spread over the large MXene flake. The exfoliated MXene undergone different heat treatment (evaporation and freezing) before filtration process (Scheme 1). According to the R. Bian *et al.* the freezing process induce the foxtail grass pattern in MXene composition which is agreed with Fig. 3c. According to our observation, the exfoliated MXene accumulates together, which cannot be used in solid composite preparation beforehand, and should be dispersed in a suitable solvent (Fig. 3c, and S1j–l of the ESI†).[44] The incessant exfoliation of MXene finally yields non-layered by-product, where we can predict the basic mechanism of MAX phase and MXene formation (Scheme 2). Further, the MXene made up of different size of layers and breaks in to the flakes during exfoliation process, and leaves the mark identified by Z on the origin. The marks X and Y indicate that cubic-like structure is formed during the MAX phase formation, and the exfoliation process exhibits the basement of the MAX phase. Further, corrosion also happens during the etching process (Fig. 3a and d). There are some cleavages present in the big by-product that is due to the etching process and settled down

during centrifuging process, leaves exfoliated MXene flake in the supernatant (Fig. 3c and d). The supernatant is used to prepare d-MXene and these can be confirmed by using XRD in which the by-product resembled MAX phase, while possessing weak 002 peak at 9° confirmed presence of residual MXene (un exfoliated) (Fig. 8a).

The SEM images of conductive polymers shows different morphology (Fig. 4a–f). The PpAP image illustrates that the formation of highly porous interwoven network structure and resembles a cross-section of wood. The plate like irregular shape PANI, PANI–PpAP, and PPy stack together and seems like exfoliated d-MXene (Fig. 4b–d and S1j†).[36–38] The PTh possesses internal cavity within the particle, and small particles accumulate on the big particle, although obvious surface cavity is presented on the surface of the particle (Fig. 4e and f). In addition, the morphology of the conductive polymers depend the type of the oxidation agent and surfactant used.[38] Moreover, the conductive polymers were invisible with the same morphology in the composites, in which it is believed that the conductive polymer mixed well with other ingredients in the composite.

The CCNW consists of irregularly arranged carbon fibre, which consists of cracks and defects. The cracks and defects are drawbacks, because they reduce the conductivity of carbon fabric. Hence, the EMI shielding of the composite is comparatively reduced. The functionalization of CCNW diminishes the defects, and enhances the conductivity and EMI shielding. In addition, the surface of the fibre of CCNW can be modified by various activities, such as coating of the carbon nanotube,
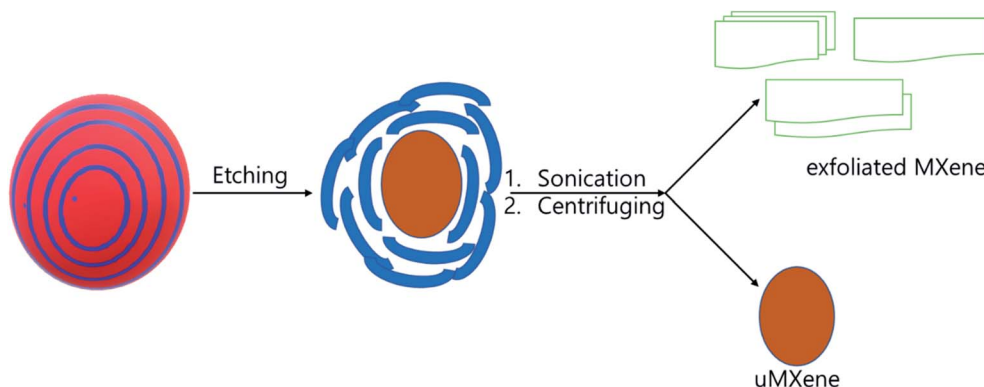
Scheme 2 The exfoliated MXene synthesis from MAX phase.

MXene, graphene, nanoparticle, and functionalization. In addition, the introduction of foreign nano-elements helps to interconnect the fibres, minimizes the defects, fills the cracks, and closes the cavity, which factors greatly influence the EMI shielding of the carbon fabric.[45] Fig. 5 shows the topology of the composites, in which Fig. 5a, b, and f display coral-like structure, while Fig. 5c exhibits morphology like a bacterial colony. In general, the surface of the composite seems rough, due to the presence of MXene and polymers. The MXene are interconnected by polymers in which conductive polymer-based composite shows prominent differences in connection of MXene, compared with MXPAT. The MXPAT surface only consist the MXene flake while conductive polymers interconnect the surface MXene and form rough appearance. Nonetheless, the connection generates groves and cavities in the composite (Fig. S1a–i of the ESI†). The polypyrrole-based MXene composite consists of hole which creates nest-like edifice and

same structure is absent in other polymer composites. In addition, each hole has extra holes that indicate the structure of ant farm (Fig. 5d and S1e of the ESI†). The d-MXene and PAT composition, rMXPAT and MXPATPN create surface cavities and grooves, whereas rMXPAT shows slightly deeper cavities, and MXPATPN have a narrow and deep groove structure, which contributes to a surface of multiple reflections (Fig. 5e and f, and S1e–i of the ESI†). In general, the surface of dMXPAT seems like an amoeba, for which phenomenon d-MXene flakes are responsible for and formed surface non-continuous MXene film, create amoeba structure (Fig. S1h of the ESI†).[14,46,47] Furthermore, the MXene flake in the composite possesses similarity with exfoliated MXene, which indicates that the exfoliation happens during the composite preparation. The polymers, $FeCl_3$, DI water, and other components in the mixture induce the delamination process (Fig. 5a–f, and S1j–l of the ESI†).
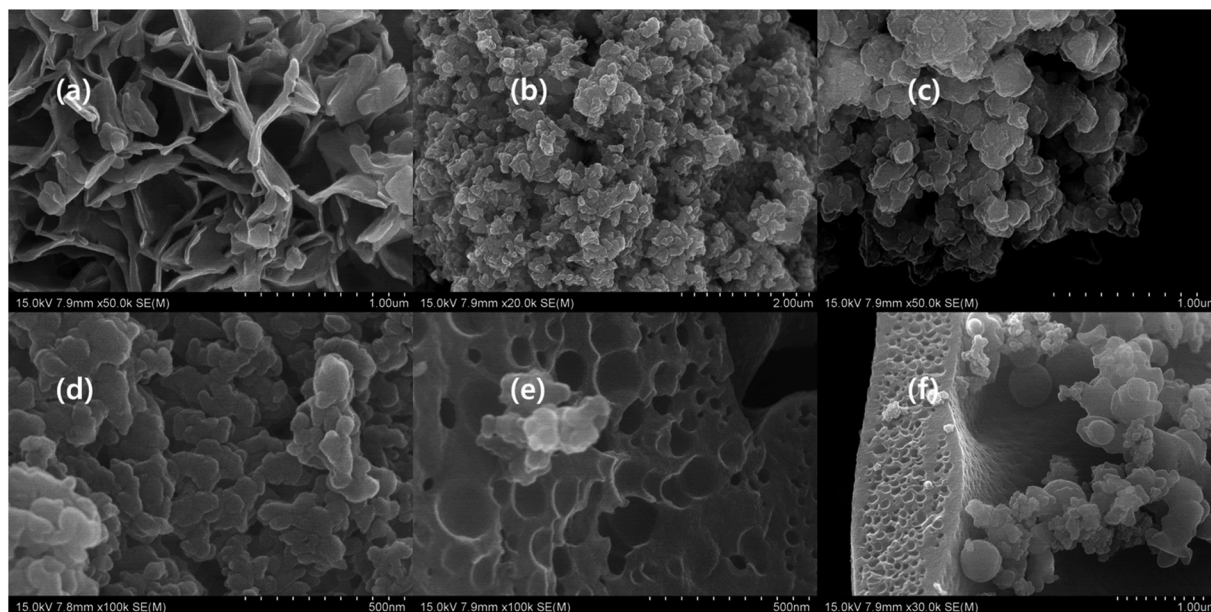

Fig. 4 SEM image of (a) PpAP ($\times$50 000), (b) PANI ($\times$20 000), (c) PANI–PpAP ($\times$50 000), (d) PPy ($\times$100 000), (e) PTh ($\times$100 000) and (f) PTh ($\times$30 000).
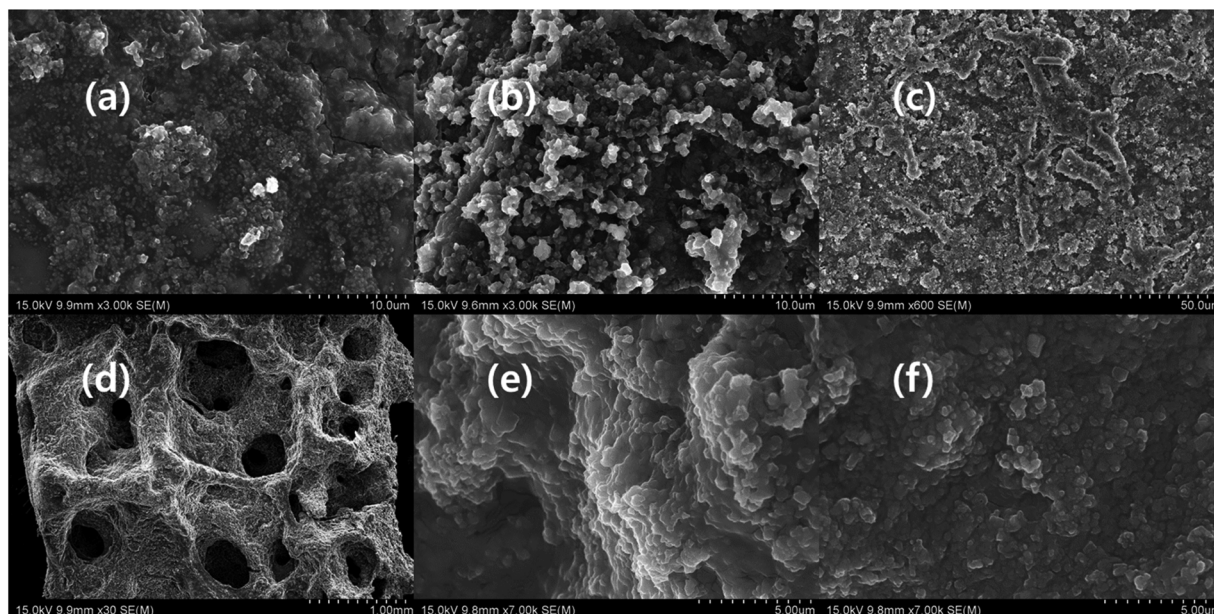
Fig. 5 SEM image of (a) MXAPPN (×3000), (b) MXAPPA (×3000), (c) MXAPPNPA (×600), (d) MXAPPY (×30), (e) d-MXAP (×7000), (f) r-MXAP (×7000).

Fig. 6, and S2 of the ESI† show the cross-section of the composites. The CCNW is sandwiched between MXene-polymer composite (Fig. 6a, and S2a, d, and e†). The carbon fibres are arranged in parallel, and induce cavity formation in the circumference of fibres (Fig. S2a, d, e and g–i of the ESI†). The cross-section of the carbon fibre consists of delaminated MXene flakes that confirm the Raagulan *et al.* study, where MXene flake was intercalated with carbon nanotube, and possessed similar structural features (Fig. 6b and c).[45] Furthermore, this implies the polymer composition based-

exfoliation occurs during the MXene–PAT composition preparation. The cross-section of MXPATPPy shows long tunnel, which indicates the internal structure resembles the ant farm, whereas rMXPAT composite consists of honeycomb cage (Fig. 6d and f). The composites exhibit many wave-like layers and F. Shahzad *et al.* reported that is due to the restacking of the MXene (Fig. 6e, and S2a–i of the ESI†), where multiple reflections are promoted (Section 3.6).[14,45] The uMXPAT displays blade-like structure that is due to the presence of u-MXene, which was absent in the other composites (Fig. S2g
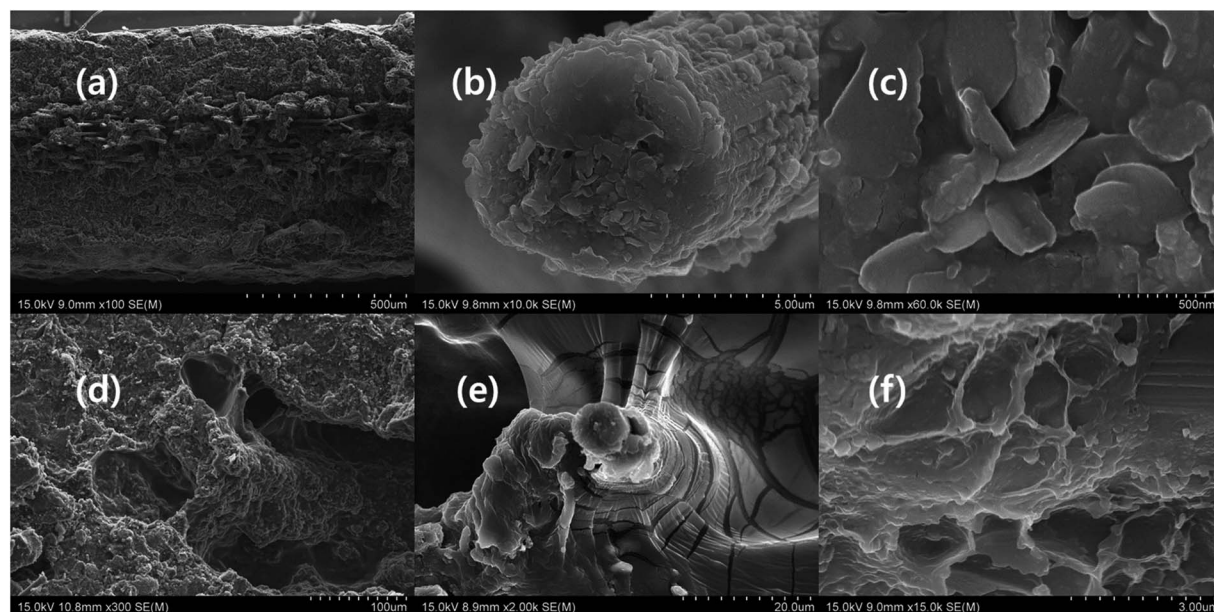

Fig. 6 Cross-section of composite (a) MXAPPA, (b) MXene on carbon fiber (×10 000), (c) MXene on carbon fiber (×60 000), (d) MXPATPPy, (e) uMXPAT, and (f) rMXPAT.

of the ESI†). The cavities in uMXPAT leave continuous layered interfaces that end up in carbon fibre (Fig. 6e and S2I of the ESI†). Possessing the abovementioned structure and u-MXene leads to good thermal conductive material (Section 3.5).

3.2. X-ray photoelectron spectroscopy (XPS)

The XPS is used to explain the surface elemental composition, structures, defects, functional groups, and bonding nature of compounds. The Gaussian–Lorentzian function of Origin Pro® is utilized to plot the fitting and overlapping curve of MXene and composites. The fitting curve of MXene gives various information about the bonding nature and functional groups of MXene. The different peak positions of O 1s, F 1s, C 1s and Ti 2p, of the $Ti_3C_2T_X$, are shown below (Fig. 7a–d).[48–51] The functional groups, such as TiO_2, $C–Ti–O_x$, Al_2O_3, and H_2O of O 1s give rise to the peaks at (529.6, 531.1, 532.3, and 533.8) eV, respectively (Fig. 7a). The single peak of F 1s at 685.5 eV is due to the $C–Ti–F_x$ functional group (Fig. 7b). The $C–Ti–T_x$, C–C, and CH_x–CO functional groups of C 1s engender the peaks at (281.1, 283.2, 284.5, and 286.1) eV which indicates presence of the C–Ti and C–C bonds (Fig. 7c). The peak positions at (454.5, 456.4, 458.5, 461.3, and 464.5) eV for (Ti–C ($2p_{3/2}$), Ti^{2+} ($2p_{3/2}$), TiO_2 ($2p_{3/2}$), Ti^{2+} ($2p_{1/2}$), and TiO_2 ($2p_{1/2}$)), respectively, are responsible for the functional groups attached to the Ti 2p environment, confirms the presents of Ti–C, Ti–O and Ti^{2+} bonds (Fig. 7d).[50,52] Thus, MXene consists of Ti–C, Ti–O, Ti–F, C–C, and C–O, hence MXene is formed with the formula Ti_3C_2(OH, F). Further, presence of Ti–C and Ti–O bond confirm the pure MXene formation and –OH and F terminal endorse the MXene with hydrophilic in nature and negative charge on the surface. The existence of the polar surface functional groups in MXene are introduced during etching process and endow good dispersibility in water, polar solvent and polar polymer.[12,13] In this study, PAT composition, NMP, water and other polar composition have been used to prepare the composites. The XPS survey of composite confirms the presence of elements, such as Fe, F, O, Ti, N, C, Cl, and S, in which N comes from PPy, PANI, PpAP, PANI, and PANI–PpAP, while S is derived from polythiophene. The MXene is the source of F, O, Ti, and C. Fe and Cl get into the composite due to the addition of $FeCl_3$ and a small amount from MXene surface functionality (Fig. 7e). XPS of Ti_3AlC_2 consists of the prominent peaks at (117.5, 284.2, 396.6, 457.8, 529.3, 975.0) eV, and extra peaks at point L at (73.3, 61.4, 35.8 and 20.5) eV (Fig. 7e). The etching process engenders extra peaks at (684.1 and 828.8) eV, whereas the point M of MXene peak at 35.8 eV remains the same with the new peak at 59.6 eV, and other peak of L disappear. The exfoliation process eliminates the common peaks of MXene and MAX phase at 457.8 eV, although peaks at point M of MXene disappear, and form new peaks at N (df-MXene) (Fig. 7e). During the evaporation drying, the exfoliated MXene turns white, and the point N shifts to the lower binding energy (db-MXene) (Fig. S4†). To eliminate the burning, the evaporation process was used to reduce the volume of the colloidal solution, then, freezing and filtration was performed. If the exfoliated MXene undergoes evaporation, freezing and filtration processes, the peak position of N

shifts to higher binding energy of point P (Fig. 7e). These peaks are helpful to identify the temperature based process of MXene. The by-product (u-MXene) also exhibits similar behaviour of d-MXene under XPS, which can be further explained by using XRD (Section 3.3). The overlapping curve of F 1s, O 1s, and C 1s indicates different peak positions, which implies that the effective interaction occurred between polymers and MXene (Fig. 7g and h, and S3 and Tables S1 and S2 of the ESI†).

3.3. X-ray powder diffraction (XRD) analysis

The XRD profile is exploited to elucidate the crystalline or amorphous nature of the material based on peak position, height, and width. Fig. 8a and b show the XRD profiles of the Ti_3AlC_2, $Ti_3C_2T_x$, exfoliated MXene and composites, and draws a 2θ range between (5 and 90)°. The sharp peaks confirm that the MAX phase and MXene derivative are crystalline in nature and all the composite holding sharp peaks, implying the crystalline behavior of the composites. The crystalline MAX phase generates sharp 2θ peaks at 9.52° (002), 19.53° (004), 34° (101), 35.1° (102), 36.8° (103), 38.99° (008), 41.76° (104), 42.54° (105), 48.48° (107), 52.36° (108), 56.5° (109), 60.16° (110), 52.36° (1011), 64.98° (1011), 70.34° (1012), and 74.02° (118), and the interplanar crystal spacing of 2θ peaks at 9.52° is 9.72 Å.[50,52–58] The etching process of the corresponding MAX phase eradicates or shifts peaks, and the sequence of new diffraction peaks is also formed. The formed MXene holds a crystalline nature, and the 2θ peak at 7.14° (002) is a characteristic peak of the MXene interplanar crystal spacing of 12.46 Å. In addition, the 2θ peaks initiating at 14.36° (111), 19.12° (200), 25.3° (101), 25.7° (110), 28.98° (220), 38.86° (222), and 40.9° (400) confirm the crystalline nature of the MXene, and attest to the occurrence of the etching process and formation of "accordion" structure. In addition, the etching process increase the interplaner space considerably. The peaks at 25.3° and 25.7° confirm the existence of TiO_2 anatase and rutile, respectively (Fig. 3a and 5a).[14,24–27,50,56,57] Moreover, peaks at 25.3° and 25.7° agree with XPS result (Fig. 7a–d). The exfoliation process mainly shifts the 7.14° peaks of MXene to lower refraction angles of (6.42 and 6.75)°, which corresponded to df-MXene and d-MXene, respectively. Further, most of the peaks of both df-MXene and d-MXene overlap each other. In addition, df-MXene engenders non-overlapping weak peaks at (12.98, 19.69, 12.44, 22.88, 26.40, and 33.11)°, while d-MXene exhibits non-overlapping peaks at (12.44, 13.94, 17.94, 22.88, and 27.84)°. These peak positions differ slightly, and evaporation process causes this slight change in 2θ value (Fig. 8a, and S5a and b†). Therefore, the df-MXene and d-MXene can be differentiate by using these characteristic peaks. The XRD profile of u-MXene and MAX phase comprise almost similar Bragg's angle, and the small humps at $2\theta = 9.5°$ indicate that it holds slight MXene property. The SEM image of u-MXene confirms the above statement (Fig. 3d). Even though u-MXene does not display a layered structure (Fig. 3d), it cannot be used to synthesize MXene. The functionalization of CCNW alters the peak position and erases some peaks of CCNW, where it shows
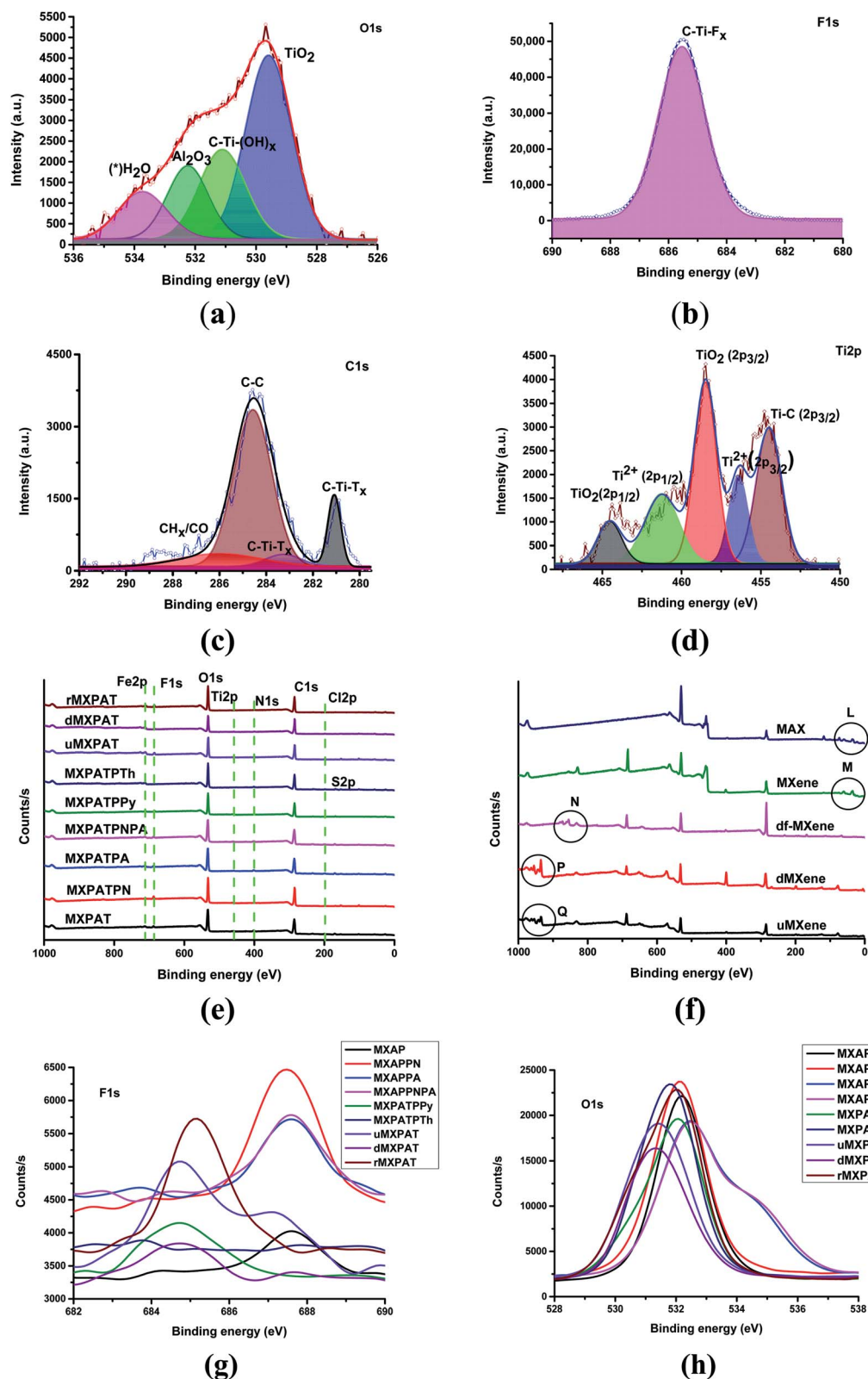
Fig. 7 XPS fitting curves of (a) O 1s, (b) F 1s, (c) C 1s, and (d) Ti 2p, (e) and (f) overlapping curve of survey, (g) overlapping curve of F 1s, and (h) overlapping curve of O 1s.

amorphous 2θ peak at 25.52°. In addition, the respective peak confirms the presence of carbon nanotubes and graphite structure in CCNW (Fig. S5c of the ESI†).[58]

Fig. 8b displays the XRD graph of the composites, in which broad peaks and sharp peaks are observed. The broad peak at 20° is due to the FCCNW and agar in the composites, which
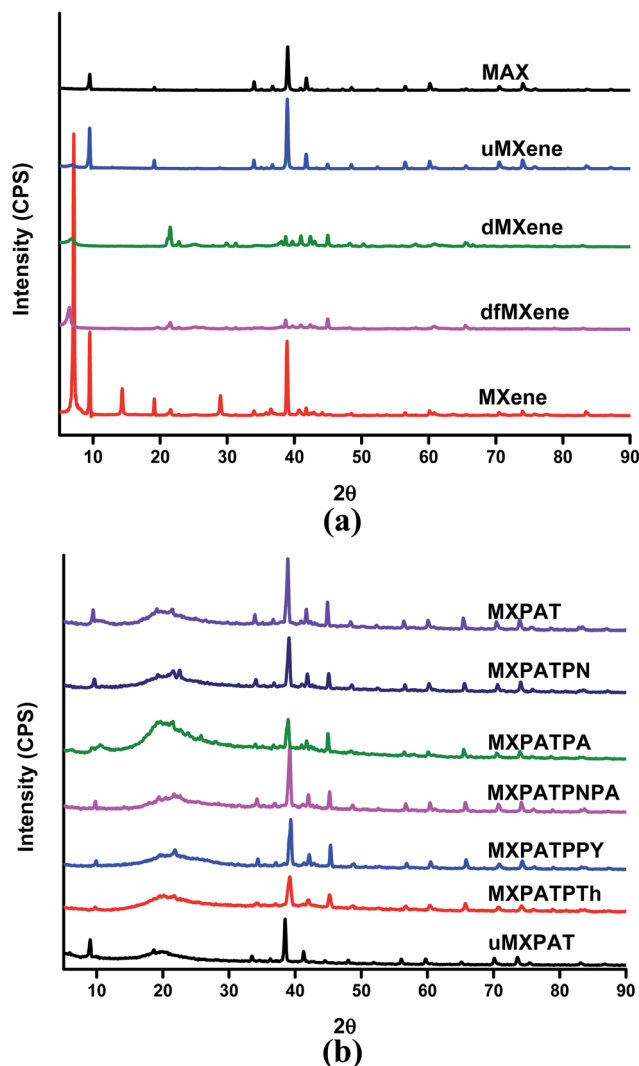
Fig. 8 XRD profile of (a) MXene, exfoliated MXene and MAX phase, and (b) composites.

imply amorphous property remains in the composites, is due to the FCCNW[45,59] (Fig. S5c and S6a–h of the ESI†), even though all the composites display many sharp peaks indicating the crystalline behaviour of the composites, which is due to the conductive polymers, MXene, and other compositions. On the whole, the composites are a crystalline in nature and the peak at about 40° confirm the presence of MXene in all composites. The Bragg angles at (18.4, 21.6, and 25.9)° designate that PANI retains its identity in MXPATPN, and the weak 25.9° peak confirms the presence of orthorhombic unit cell with (200) reflective plane of PANI.[60,61] The peaks at (19.6, 21.6, 23.9, and 25.8)° specify the existence of PpAP, in which the characteristic weak peak at 25.8° verifies the occurrence of stacks of poly aminophenol rings, and the hydrogen bond between MXene and polymers diminishes the intensity of the peak.[37,62] The distinctive Bragg angles 2θ at (19.37, 20.47, 21.57, 22.67, and 25.3)° peaks confirm the PANI–PpAP copolymer. The typical diffraction angles at (19.53, 21.92, 25.3, and 25.9)° confirm the availability of PPy in MXPATPPy, and the combination of these

peaks suggest the amorphous nature of PPy.[63–65] The broad peak that appears between (16.5 and 30)° assures the existence of polythiophene.[66,67] The characteristic 2θ at (5.94, 8.98, 18.57, 19.84, and 38.38)° indicate the presence of u-MXene, and other peaks confirm the u-MXene intercalates well with polymer and FCCNW matrix. The MXPAT, MXPATPN, MXPATPA, MXPATPNPA, MXPATPPy, MXPATPTh, and uMXPAT own specific Bragg angles that are (9.79, 10.57, 9.88, 9.88, 9.94, 9.79, and 8.98)°, respectively. These slight differences guarantee that the interaction between polymer matrix and fillers was effective and can be identified the particular composite (Fig. 8b, S6a–h and Table S3 of the ESI†).

3.4. Raman spectroscopic analysis of composites

The Raman spectrum is the non-destructive and time-resolving tool that is utilized to investigate the structural feature, level of defects, crystalline nature, and physicochemical behaviour of the materials, such as graphene, MXene, carbon fabric, CNT, nanoparticles, and composites that can be studied using Raman spectroscopy.[3,14,68] Fig. 9a and b show the Raman spectra of MXene, MAX phase, CCNW, and composites, which are plotted in the (0–4000) cm^{-1} Raman shift range. The in-plane mode of Ti gives rise to the peak at 394 cm^{-1}, despite the fact that the peaks at (624 and 263) cm^{-1} are ascribed to surface functional groups and C, respectively. Furthermore, the weak peaks at (1353 and 1568) cm^{-1} specify the corresponding D and G bands of $Ti_3C_2T_x$, while the (624, 510, and 398) cm^{-1} Raman shifts confirm the existence of TiO_2 anatase and XPS and XRD results agree with this statement (Fig. 7a–d, 8a and 9a).[53,54,57] Moreover, the disappearance of the peak of Ti_3AlC_2 at 263 cm^{-1} guarantees the depletion of A layer, and the introduction of surface functionality in the place of Al-linked Ti and C. This change implies the formation of MXene with –OH and F functional groups. The prominent peaks at (1363 and 1592.1) cm^{-1} are labelled as the D and G bands of CCNW, which infer the presence of highly oriented pyrolytic graphite (HOPG), and the weak G′ band at 2908.2 cm^{-1} represents the occurrence of graphite-like structure in CCNW (Fig. 9a).[45]

The composites exhibit similar behavior, and the spectra are plotted in the (0–4000) cm^{-1} range. The origin of the composite in the Raman spectra varies, while MXPATPA and MXPATPTh of the minimal point originate at a similar point. MXPATPN, MXPATPA, MXPATPNPA, MXPATPPY, and dMXPAT display characteristic peaks at (1603.93, 1597.79, 1608.20, 1566.89, and 1761.03) cm^{-1}, respectively, which imply that the G band of MXene peak is shifted, and the corresponding peak is absent in the other composites. This phenomenon hints that effective interaction happened between MXene and polymers. The distinctive peaks at (984.11 and 1049.67) cm^{-1} indicate the polypyrrole based composite, whereas (2238.50 and 3163.90) cm^{-1} confirm the presence of r-MXene (Fig. 9b, and S7a–h of the ESI†), by which the MXPATPPy and rMXPAT composite can easily be identified. The peaks at (412.73, 824.03, and 883.7) cm^{-1} of MXPATPN arise due to the in-plane and out-of-plane vibration mode of protonated PANI, and the weak peak at 1375 cm^{-1} confirms that the PANI displays less electric
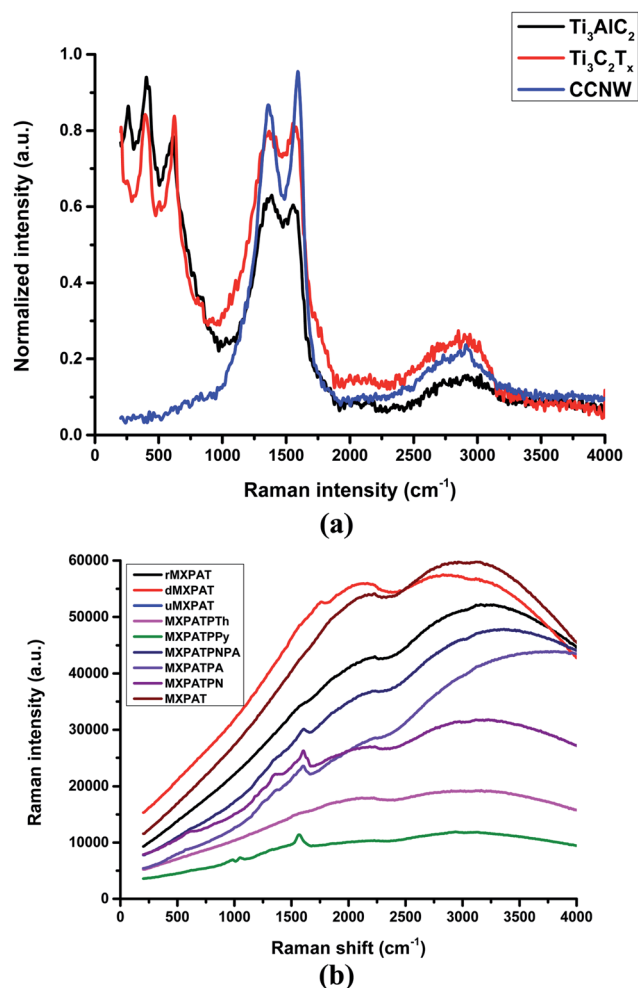
Fig. 9 Raman spectroscopy of (a) composite, and (b) MXene, MAX phase, and composite.

conductivity (Fig. 9b, S7c and d of the ESI†).[69] The band in the 1602.49 cm^{-1} region engrains the stretching frequency of the C–C bond of PANI.[70] In addition, the peaks in the range (800–1000) cm^{-1}, such as (824.03 and 883.7) cm^{-1}, affirm the presence of agar.[71] The band at 1135.95 cm^{-1} can represent the stretching mode of bonds such as C–O and C–C of PVA. The peaks at (1179.66 and 1431.69) cm^{-1} represent the stretching frequency of –C–H and –OH of PVA (Fig. 9b, and S7a–h of the ESI).[72] According to Kumar *et al.*, the trimesic acid can be confirmed by characteristic peaks at 1648 cm^{-1}(C=O), 955 cm^{-1} (–OH–vibration) and 3085 cm^{-1} (–OH-stretching). The peak of C=O at 1651.9 cm^{-1} confirms the existence of trimesic acid, and the absence of the other two peaks shows that the trimesic acid bonds successfully with PVA and agar (Fig. 9b and S7c–e†).[73] In addition, the weak peaks of CCNW and MXene virtually disappear, which specifies that effective interaction has occurred among MXene, PANI, agar, PVA, and the other compositions (Fig. 9b, S7b–h and Table S4 of the ESI†). The MXPATPNPA overlaps with MXPATPN in about the 60 cm^{-1} range, while MXPATPA aligns in parallel up to 1000 cm^{-1}, which designates the presence of PANI–PpAP (Fig. 9b, and S7c of the

ESI†). MXPATPN shows characteristic peaks within 1000 cm^{-1}, and the MXPATPA also exhibits similar peaks at (419.35, 571.25, and 798.92) cm^{-1}, even though MXPATPNPA do not reveal typical peaks in this region, but disclose distinctive peaks at 1341.16 cm^{-1}. Further, the distinguishing peaks at 1603.93 cm^{-1} confirm the presence of MXPATPN, MXPATPA, and MXPATPNPA (Fig. 9b, and S7b–d†). The MXPATPPy engenders distinctive bands at (924.8, 984.11, 1049.67, and 1566.89) cm^{-1}, in which (924.8, 984.11, and 1049.67) cm^{-1} are considered as the ring deformation of quinoid polaronic, bipolaronic structure, and C–H in-plane deformation of pyrrole, respectively. The peaks at (701.24 and 1450.06) cm^{-1} confirm the C–C and C=C stretching frequency of MXPATPTh.[74,75] The range of (250–1500) cm^{-1} of MXPAT, rMXPAT, dMXPAT, and uMXPAT exposes a linear trend, and exhibits distinctive peaks at (2225.06, 2228.48, 1761.03, and 2114.83) cm^{-1}, by which the corresponding composites can be identified (Fig. 9b and S7†). Furthermore, the disappearance of the D and G bands of MXene and CCNW indicates that operative bonding and interaction have occurred between them, and formed perfect composite.

3.5. Thermal and electric property of the composites

3.5.1. Thermal stability and thermo gravimetric analysis of composites. The thermogravimetry analysis (TGA) and differential thermal analysis (DTA) were exploited to examine the thermal stability of the composite under a particular temperature range. The TGA and DTA analyses were carried out using Al$_2$O$_3$ crucible in a nitrogen environment (flow rate of 50 mL min^{-1}) with a heating rate of 10 °C min^{-1}. Fig. 11a and b show the TGA and DTG graphs, and all the composites display similar behaviour in both cases, with outstanding thermal stability. It was obvious that the weight loss of the composite varies, due to the constitutional composition effect of composites. The DTG plot displays several peaks that correlate with the endothermic and exothermic peaks of DSC, where the weight loss of the composite happens.[76] The composite undergoes about 15% weight loss in the temperature range (30–175) °C. Even though the level of weight loss varies according to the constitutional components of the composites, MXPAT, MXPATPN, MXPATPNPA, MXPATPPy, MXPATPTh and uMXPAT lose (16.81, 14.71, 13.37, 13.86, 14.33, 13.65, and 13.69) % of weight, respectively, and the corresponding temperatures are (194.17, 194.81, 190.77, 194.17, 180.14, 176.52, and 185.45) °C, respectively. The total reductions of weight of MXPAT, MXPATPN, MXPATPNPA, MXPATPPy, MXPATPTh, and uMXPAT are (65.69, 58.86, 56.67, 55.09, 66.11, 63.54, and 59.05) %, respectively, in the entire temperature range of (30–1000) °C (Fig. 11a and b, and S8a–h and Table S5 of the ESI†). Among all the composites, MXPATPPy shows a maximum of 66.11% of weight loss, while MXPATPNPA shows a minimum of 55.09%. The PANI–PpAP co-polymer minimizes the thermal degradation, which is due to the hydroxyl and amine groups in polymer. On the other hand, the PPy also shows that nitrogen displays the highest degradation. Thus, these prominent differences are due to the copolymer effect. In addition, the thermal stability of the composite can also be explained by using heat-resistance

index (T_s) which can be calculated from the TGA value of the composites. The T_{d5} (5% of weigh loss) and T_{d30} (30% weight loss) can be derived from TGA and the T_s can be calculated by using the equation that is $T_s = 0.49[T_{d5} + 0.6(T_{d30} - T_{d5})]$. The T_s reveals that how far the composite resists the thermal degradation and fire-retardant material have higher T_s value.[26and77] The all the composites show the T_s value above $\sim$95 °C in which MXPATPA exhibits higher T_s value whereas MXPATPPy displays lower value. The T_s result shows that the MXPATPA resist thermal degradation more while MXPAPNPA exhibits less thermal degradation in entire temperature range (Fig. 10a and Table 2).

3.5.2. Thermal conductivity, thermal diffusivity, and heat capacity analysis of the composites.

There are many types of thermal conductivity measurement methods which can be categorized into two, those are steady-state measurement method and non-steady-state measurement method. The guarded hot plate method and guarded heat flow meter method are included in steady-state measurement methods while laser flash, transient plane source, temperature wave analysis, hot wire and line source probe method fall into non-steady-state method. In addition, the transient line source method is very
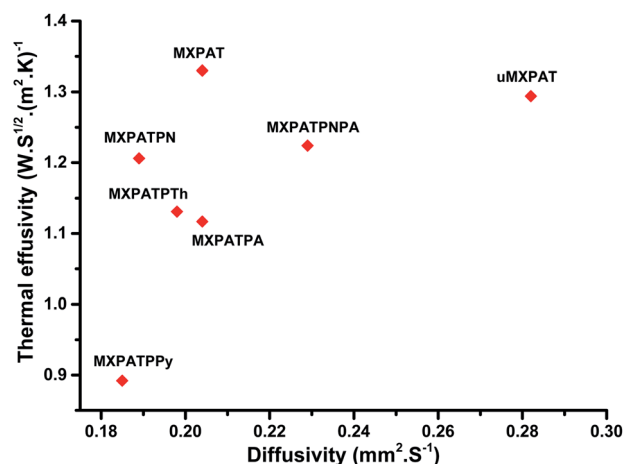

Fig. 11 Thermal effusivity against diffusivity.

Fig. 10 TGA and differential thermal analysis (DTA) analysis of the composites (a) TG of composite, and (b) DTG of the composites.

fast method and can be used to measure molten and solid sample which is the advantage of transient line source method compare to another non-steady-state method stated. The steady state measurement is often time consuming and need demanding experimental conditions such as temperature control, specific dimension for sample and adiabatic environment. But the non-steady state measurement is more advantageous than steady-state measurement which is due to short measurement time, no rigorous environmental conditions and high accuracy.[78] The thermal diffusivity, thermal conductivity, and heat capacity were obtained by NETZSCH LFA analyzer. For the investigation of thermal diffusivity, thermal conductivity, and heat capacity, LFA 467 instrument was used with 8.89 mm of spot size, diameter of 12.500 mm, LFA 467 steel furnace with 12.7 mm sample holder. All the analyses were performed under nitrogen environment with 60 mL min^{-1} purging rate and 20 mL min^{-1} protective flow rate. The thermal conductivity (TC) can be calculated according to eqn (1),[79] where k is the thermal conductivity, m is the mass of the sample, C_p is the specific heat capacity of the sample, (dT/dt) is the cooling rate, X is the thickness of the sample, A is the cross-section of the sample, and $t_2 - t_1$ is the temperature difference between the opposite surfaces of the sample. The SI unit of K is W (m K)$^{-1}$. The thermal conductivity confirms through the various strategies that they are photon, phonon, and charge carriers. The high temperature gives rise to the photon conductivity, whereas atomic collision leads to a lattice vibration bringing about
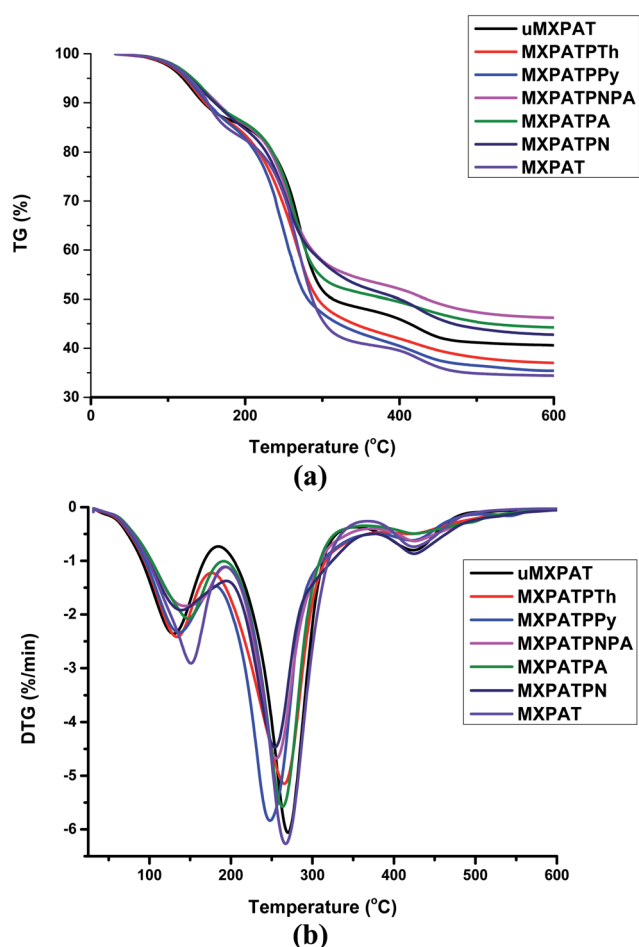
Table 2 Heat-resistance index (T_s) of the composites

Composites	T_{d30}	T_{d5}	T_s (°C)
MXPAT	252.78	127.59	99.33
MXPATPN	254.30	128.26	99.90
MXPATPA	259.58	131.71	102.13
MXPATPNPA	257.64	130.71	101.37
MXPATPPy	240.00	124.33	94.93
MXPATPTh	247.92	122.22	96.84
uMXPAT	262.22	119.44	100.50

phonon conductivity. The above-mentioned phenomena cannot act concurrently, even though one governs the others, which is determined by the atmosphere of the material used. In addition, TC can be indirectly estimated by using Fourier's law, where k is TC, α is the thermal diffusivity, C_p is the heat capacity, and ρ is the density of the material (eqn (2)). Further, the Parker formula is used to calculate the thermal diffusivity, where d is the thickness of the sample, and $t_{0.5}$ is the time duration of the laser pulse to reach half of the maximum temperature (eqn (4)–(6)).[79–81]

$$k = \frac{mc\left(\frac{dT}{dt}\right)X}{A(t_2 - t_1)} \tag{1}$$

$$k = \propto C_p\rho \tag{2}$$

$$\alpha = 1.38\frac{d^2}{t_{0.5}} \tag{3}$$

The thermal effusivity e is the capability of transmission of the thermal energy to the surroundings, and is equivalent to the square root of the multiplication of the thermal conductivity, density, and heat capacity of the composite (eqn (4)–(6)).[81,82]

$$C_p = \frac{\Delta Hm}{\Delta T} = \frac{\Delta Hm}{T_{end} - T_{onset}} \tag{4}$$

$$e = \sqrt{k}\rho\Delta H8\Big/\sqrt{\Delta T} \tag{5}$$

$$e = \sqrt{k}\rho C_p \tag{6}$$

Table 1 shows the thermal diffusivity, thermal conductivity, heat capacity, thermal effusivity, density, and thickness of the composites, and the corresponding ranges are (0.185–0.282) mm^2 s^{-1}, (0.384–0.687) W (m K)$^{-1}$, (1.889–2.247) J (g K)$^{-1}$, (0.892–1.330) W s$^{1/2}$ (m^2 K)$^{-1}$, (0.988–1.336) g cm^{-3}, and (0.04–0.16) cm, respectively. The MXPATPPy and uMXPAT display the minimum and maximum thermal diffusivity, whereas the corresponding thermal effusivity is (0.892 and 1.294) W s$^{1/2}$ (m^2 K)$^{-1}$, respectively. The 1.330 W s$^{1/2}$ (m^2 K)$^{-1}$ of MXPAT discloses the maximum thermal effusivity, while 0.892 W s$^{1/2}$ (m^2 K)$^{-1}$ is shown by MXPATPPy. uMXPAT reveals 78.9% of higher thermal conductivity, compared to MXPATPPy, even though MXPATPPY

demonstrates 11.12% higher heat capacity, compared with uMXPAT. The MXPATPPy shows lower density, which is directly correlated to the thermal diffusivity, thermal effusivity, and thermal conductivity, which show lower values of α, k and e (Table 3). The e containing materials can be utilized for various applications, such as intelligent textiles, waste thermal harvest, thermal sensors, etc. The operative thermal energy garnering material should be phase-changing material (PCM), which can be confirmed by using thermal analysis, where exothermic and endothermic peaks can be predicted from the DTG profile. All the fabricated composites demonstrate phase changing ability and e (Fig. 10b). Hence, the composites can be utilized for thermal energy storage purpose.[81,83] Fig. 10 shows that the uMXPAT reveals higher k and relatively higher e. uMXPAT can be used for thermal storage, compared to the others. In addition, the by-product of MXene can be utilized for thermal energy storage process. In addition, the thermal energy can be converted into the electrical energy for which Thermoelectric Module (TEG) is used. The developed temperature variation creates the electrical potential between hot and cold junction which can be converted into electrical energy know as Peltier effect. This phenomenon can be explained by using seebeck concept that is $V = \alpha(T_h - T_c)$ where V is voltage $(T_h - T_c)$ temperature differences between hot and cold junction and α is seebeck constant. Further, the temperature variation between surfaces lead to charge carrier flow, produce the electricity. Hence, the thermal energy of the composite can be converted into electrical energy.[84,85] The Kang et al. reported that Ti$_3$C$_2$/epoxy (0.2 wt%) composite produced 0.122 mm^2 s^{-1} of thermal diffusivity, and 0.270 W (m K)$^{-1}$ of thermal conductivity whereas pure epoxy displayed 0.110 mm^2 s^{-1} and 0.243 W (m K)$^{-1}$ of thermal diffusivity and TC, respectively.[86] The introduction of the MXene into the polymer enhance the thermal diffusivity and TC. Hence, the composites shown in Table 3 exhibit excellent thermal diffusivity and TC, compared to Ti$_3$C$_2$/epoxy composite. The in-plane TC of Ti$_3$C$_2$T$_x$ film discloses the (1.26 and 2.84) W (m K)$^{-1}$ at (80 and 290) K, respectively. The MXene/PVDF (5 wt%) manifests 0.363 of TC, which is lower than that of the composite fabricated in this study. Therefore, composite exhibit excellent thermal property and can be used as the thermal conductor (Table 3).[87]

3.5.3. The electric conductivity (EC) of the composites. The electric conductivity (σ) can be calculated from the factors such as resistance (R), resistivity (ρ), the cross-section ($A = wt$, where

Table 3 Thermal diffusivity, conductivity, heat capacity, and density of composite

| Composite	Diffusivity mm^2 s^{-1}	Thermal conductivity W (m K)$^{-1}$	Heat capacity J (g K)$^{-1}$	Density g cm^{-3}	Thermal effusivity W s$^{1/2}$ m^{-2} K^{-1}
MXPAT	0.204	0.600	2.247	1.312	1.330
MXPATPN	0.189	0.524	2.078	1.336	1.206
MXPATPA	0.204	0.504	2.033	1.217	1.117
MXPATPNPA	0.229	0.586	1.997	1.281	1.224
MXPATPPy	0.185	0.384	2.099	0.988	0.892
MXPATPTh	0.198	0.504	2.028	1.252	1.131
uMXPAT	0.282	0.687	1.889	1.291	1.294

w is width and t, is thickness), length (L) and sheet resistance (R_s). The arithmetic multiplication of resistivity and length divided by cross-section gives rise resistance ($R = (\rho L)/A$) of the materials. The multiplied value of R_s and t produce the ρ. The conductivity of the material is reversibly proposal to ρ of the material.[45] The thickness, electric conductivity, surface resistance and resistivity of the composites are shown in Table 4. The range of the thickness of the composites is 0.4–1.6 mm which indicates the thickness of the composite in μm range. The composites display 1.6–160 000 Ω and 0.128–256 000 Ω cm range of surface resistance and resistivity, respectively. The conductivity range of the composites place between 3.906×10^{-5} and 7.813 S cm^{-1}. It was obvious that MXPATPPY showed very higher resistance and resistivity compare to other composites and exhibites very low EC value of 3.906×10^{-5} S cm^{-1}. Hence, the EMI shielding of the MXPATPPy must be very low, though, it shows 99.99% of shielding efficiency which is discussed in details in Section 3.6. In addition, the MXPATPPy exhibited low thermal diffusivity (0.185 mm^2 s^{-1}), thermal conductivity (0.384 W (m K)$^{-1}$), density (0.988 g cm^{-3}) and thermal effusivity (0.892 W s$^{1/2}$ m^{-2} K^{-1}) which indicates that the lower EC and its structure influence the thermal properties of the MXPATPPy (Tables 3 and 4, Fig. 5d, S1d and S2d†). The internal channels in the composite and surface cavities play a major role for the uncommon behavior of the composite. EC of PVA is 1.63×10^{-12} S cm^{-1} and the EC of agar is 6.5×10^{-5} S cm^{-1} which imply that the addition of CP and MXene greatly improve the EC of the composites.[88,89] Moreover, the EC of PANI,[36] PTh[90] and PPy[91] are 4.4, 7.17×10^{-6} and 0.61 S cm^{-1}, respectively, and change in EC of the composite due to the presence of the MXene. The conductivity of MXPATPN and MXPATPA was lower than that of MXPAT, even though, MXPATPNPA exhibited 1000 times higher conductivity than MXPATPN which was due to the introduction of PNPA co-polymer. Thus, PANI–PpAP copolymer have excellent conductivity and EMI shielding enhancing ability than PANI and PpAP (Table 4 and Section 3.6). The above mention phenomena happened due to the effective hole–electron transportation between MXene and PANI–PpAP. It is obvious that CP comparatively increase the EMI shielding of the composites (Section 3.6). The r-MXene and u-MXene composition held lower EC compare to MXene which is considered due to lack of proper orientation and bonding among constitutional elements, though, rMXPAT possessed 8.18 times higher conductivity than u-MXene. This is due to the availability of surface functional groups which promote bonding of fillers. The reduction process considerably replaced –F by –H in MXene and u-MXene significantly lost surface functional groups due to the exfoliation process. This process diminishes the charge flow along the matrix of the composite, thus, show lower (Table 4).

3.6. EMI shielding measurement

Electromagnetic radiation (EMR) is a transverse wave that can propagate through various materials. When EMR hits shielding materials, and undergoes transformation, such as absorption, reflection, and multiple reflections, it is called EMI shielding.
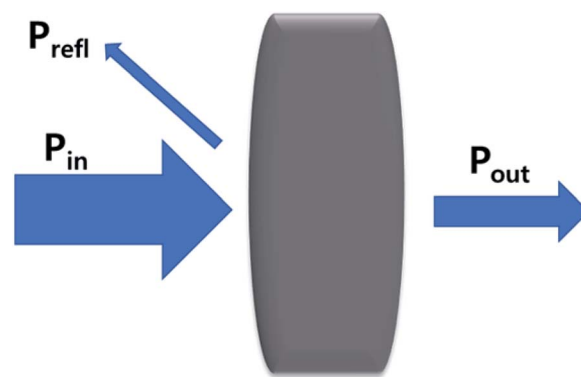
$$\text{Transmitance} = P_{out}/P_{in}$$

$$\text{Reflectance} = P_{refl}/P_{in}$$

$$R + T + A = 1$$

where, R, T, and A imply the reflection, transmission, and absorption fractions, respectively. In addition, the absorption power can be articulated as $P_A = P_{in} - P_{out} - P_{refl}$. The total EMI shielding (SE_T) can be expressed by the logarithmic ratio between the power of incoming (P_{in}) and outgoing (P_{out}) EMR radiation (eqn (7)).

$$SE_T = 10 \log(P_{in}/P_{out}) = SE_A + SE_R + SE_{MR} \qquad (7)$$

Table 4 The electric conductivity comparison of the composites

Composites	Thickness (cm)	Surface resistance (R_s Ω)	Resistivity (Ω cm)	Conductivity (S cm^{-1})
MXPAT	0.052	6.1	0.317	3.153
MXPATPN	0.087	15	1.305	0.00766
MXPATPA	0.062	13	0.806	1.241
MXPATPNPA	0.08	1.6	0.128	7.813
MXPATPPy	0.16	160 000	256 000	3.906×10^{-5}
MXPATPTh	0.092	680	62.56	0.0159
uMXPAT	0.04	270	10.8	0.0926
dMXPAT	0.06	46	2.76	0.362
rMXPAT	0.066	20	1.32	0.758

where, SE_T is the total EMI shielding, SE_A is the absorption, SE_R is the reflection, and SE_{MR} is multiple reflections. The effect of multiple reflections is insignificant, and the total EMI shielding can be expressed as $SE_T = SE_A + SE_R$. Further, the power of the incident wave (P_I) can be calculated by adding the reflected power (P_R), absorbed power (P_A), and transmitted power (P_T) that is $P_I = P_A + P_R + P_T$. In addition, the intensity can be calculated in the same way as $I_o = I_A + I_R + I_T$. The specific shielding effectiveness (SSE) is driven from the ratio between EMI SE and density (ρ) of the materials, and the corresponding unit is dB g^{-1} cm^3. It is obvious that low-density materials possess higher SSE value. Furthermore, SSE does not have the thickness (t) basis information, because of the large t with lower ρ exhibits higher SSE. Hence, absolute effectiveness (SSE/t) with the unit of dB g^{-1} cm^2 is used to evaluate the thickness effect of the material (eqn (8) and (9)).

$$SSE = \frac{EMI\ SE}{\rho} \tag{8}$$

$$SSE/t = \frac{SSE}{t} \tag{9}$$

The composites were fabricated by the spray coating process for which special polymer composition was synthesized, called PAT solution. The MXene was directly dispersed in PAT solution, while the conductive polymer was dispersed in NMP solution. Then both are mixed together, and finally utilized for the spray coating process on CCNW with areal density of 30 g m^{-2}. In the PAT solution preparation process PVDF used as a plasticizer,[92] the trimesic acid is utilized to connect both agar and PVA for the desired FeCl$_3$ used as coupling reagent.[93] The glycerin and polyacrylic acid were exploited as a dispersant and gained the strength of composite, respectively.[94,95] The PAT is hydrophilic in nature, as it consists of agar and PVA. This PAT solution was a key player to disseminate MXene evenly, and conductive polymers intercalate within MXene, which creates a conductive network. In addition to the conductive network, CP plays a major role in creating the different structural features within the composite. It is virtually true according to the SEM that reflection (SE_R) and absorption (SE_A) give rise to new phenomena for EMI shielding. In the EMI shielding, the absorption plays a major role, while reflection exposes a general trend (Fig. 11a–c and Table S7 of ESI†). The maximum, minimum, and average SE ranges of composite are ((39.33–45.18), (36.04–41.54), and (37.25–42.40)) dB, while the maximum, minimum, and average SE_R ranges are ((4.71–11.44), (2.27–9.47), and (3.24–10.13)) dB, respectively. In addition, the SE_A is prominent compared to SE_R, and its maximum, minimum, and average ranges are ((29.99–37.57), (26.24–36.46), and (27.55–36.77)) dB, respectively. The maximum EMI shielding values of MXPAT, MXPATPN, MXPATPA, MXPATPNPA, MXPATPPy, MXPATPTh, uMXPAT, dMXPAT, and rMXPAT are (41.31, 39.33, 45.18, 44.08, 41.31, 42.99, 39.69, 43.74, and 44.31) dB, respectively; and the corresponding minimum EMI shielding values are (38.55, 37.83, 39.00, 37.87, 39.65, 40.25, 36.04, 41.54, and 39.94) dB, respectively. In these results, MXPATPA

shows 45.18 dB of maximum shielding, whereas MXPATPN displays 39.33 dB of lowest EMI shielding which is due to the less conductive PANI. The minimum SE_R values of MXPAT, MXPATPN, MXPATPA, MXPATPNPA, MXPATPPy, MXPATPTh, uMXPAT, dMXPAT, and rMXPAT are (9.27, 7.40, 8.41, 7.37, 2.27, 7.87, 9.18, 8.49, and 9.47) dB, respectively, while the corresponding maximum SE_A values are (30.58, 30.44, 34.85, 36.56, 37.57, 34.87, 29.99, 34.48 and 34.09) dB, respectively. It was found that MXPATPA exhibits the higher SE of 45.18 dB, which is due to the PpAP, and the absence of PpAP reduces SE to about 10.94%. Hence, the intercalation of CP relatively alters the SE with respect to MXPAT. MXPATPNPA, MXPATPPy, MXPATPTh, and MXPATPN reveal (6.71, 0, 4.07, and −4.79) %, respectively, where a minus sign indicates the reduction of SE with respect to MXPAT. The reduction of SE in MXPATPN due to PANI can be further affirmed by the Raman band at 1375 cm^{-1} (Fig. 9b). It is apparent that the reduction of MXene increases SE by 7.26% which is another output that MXene can be reduced by LiAlH$_4$, and has an impact on EMI shielding (Fig. 11a, and Table S7 of the ESI†). The MXPATPPy has ant farm-like structure, which promotes the absorption, and surface cavities can be seen by the naked eye. Fig. 11d below shows the basic mechanism of MXPATPPy, where surface cavities act as reflection, multiple reflections, and absorption units, while MXene layers contribute as multiple reflection units, which lead to absorption, and each ant farm-like structure purely gives rise to absorption unit by internal multiple reflection process (Fig. 5d, S1e and S2e of ESI†). Hence, MXPATPPy demonstrates 23.14 times higher absorption compared to reflection. The MXPAT-PAPN shows 36.56 dB of absorption and 9.09 dB of reflection which is due to the porous conductive network of the MXPAT-PAPN. In addition, the MXPATPNPA displays higher EC of 7.813 S cm^{-1} which is due to the presence of PpAP-PANI co-polymer, has impact on reflection process. In porous structure, PpAP-PANI co-polymer induces the reflection and it turn to multiple reflection in pores which leads to absorption. The basic mechanism is similar to the MXPATPPY (Fig. 12a–d and S2d, Table 4, S8 and S9 of the ESI†). The dMXPAT and rMXPAT were studied to compare EMI shielding with MXPAT, in which rMXPAT shows higher EMI shielding of 44.31 dB, while MXPAT shows 41.31 dB with higher mechanical strength (2.88 MPa) and elastic nature compare to other composite fabricated (Fig. S9†). Tensile strength of MXene is 1.8 MPa while MXene/eggshell membrane composite shows 1.48 MPa of tensile strength which is less than that of MXPAT (2.88 MPa) and MXene.[96] In addition, the tensile strength of MXPATPPy and MXPATPN are 1.68 and 1.47 MPa, respectively, and tensile strength of MXPATPA is 4.3 MPa. The Nacre-Inspired Structure of MXene/cellulose composite displays 135.4 MPa of tensile strength. Hence, addition of PAT composition, arrangement of MXene flake in composite and presence of hydroxyl functional group in polymer significantly increase tensile strength of the composites.[11,96,97] The SSE range is (28.85–40.49) dB g^{-1} cm^3, in which uMXPAT demonstrates the lowest value of 28.85 dB g^{-1} cm^3. The SSE/t range was 236.45–721.25 dB g^{-1} cm^2 in which uMX-PAT possessed maximum value of 721.25 dB g^{-1} cm^2 (Table S7†).
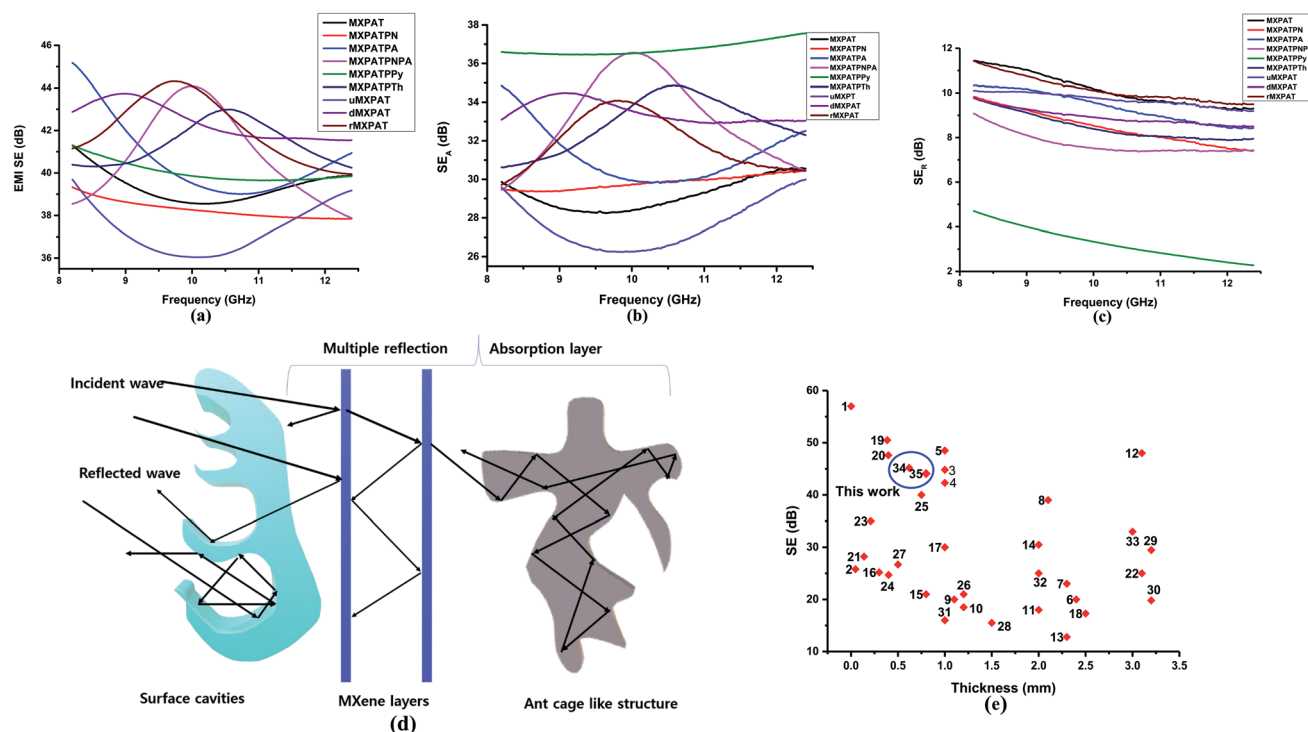
Fig. 12 EMI shielding of composite (a) SE, (b) SE_A, (c) SE_R, (d) EMI shielding mechanism and (e) EMI shielding comparison.

The SE/t is calculated by normalizing the SE value by thickness which is density free comparison among SE values.[95] The SE/t range of the composites is 1.393–1.6 dB mm^{-1} in which MXPATPA and MXPATPN possessed maximum and minimum value, respectively (Table S7†). All the composite showed 99.99% of EMI shielding effectiveness and corresponding bandwidth of MXPAT, MXPATPN, MXPATPA, MXPATPNPA, MXPATPPy, MXPATPTh, uMXPAT, dMXPAT and rMXPAT were (8.82–12.4, 8.2–12.4, 9.31–12.4, 8.2–11.98, 10.06–12.4, 8.42–12.36, 8.31–12.4, 8.24–9.72 and 8.24–11.19) GHz, respectively (Table S10†). Among all bandwidth uMXPAT held 4.09 GHz range bandwidth while dMXPAT possessed lowest of 1.48 GHz (Table S10†). The Shui. *et al.* study showed that Cu plate with a thickness of 3.1 mm exhibited 90 dB while Cu foil exhibited 70 dB with 0.01 mm of thickness.[14,98] Despite the MXene/sodium alginate composition on PET film with the thickness of 45 μm gave rise 92 dB. Hence, MXene is effective protector than Cu in tiny electronic devises.[98] The MXene/polyimide aerogel composite exhibits multifunctional properties and shows −45.4 dB of reflection loss in X-band region with 0.004 S cm^{-1} of EC, 2 mm of thickness and 0.009 g cm^{-3} of density while CNTs/MXene/cellulose displays 38.4 dB of EMI SE with thickness of 0.004 cm and 25.066 S cm^{-1}.[95,99] This is obvious that the aerogel is an efficient structure for EMI SE of MXene polymer composition. The MXene coated cotton fabric shows 48.9 dB of EMI SE with 0.00067 cm of thickness, 2969 dB g^{-1} cm^2 of SSE/t and 1570 S cm^{-1} of EC.[99] In cotton fabric the MXene underwent wrinkling arrangement which increase the EMI shielding considerably. Thus, arrangement and order of MXene stacks are important for the EMI shielding behavior of the MXene

composite.[95,99,100] The carbon fabric with 30 g m^{-2} exhibited EMI shielding of 27.14 dB and Raagulan *et al.* study showed that the functionalization significantly changes the EMI shielding of carbon fabric.[45,101] In addition, the comparison of previous work illustrated in Fig. 11f (Tables S11 and S12†). On the whole, the composites can be utilized both EMI shielding and thermal energy conversion process.

4 Conclusion

A new type of PAT composition was prepared at the optimized condition and which acts as a binder of MXene and conductive polymers. The FCCNW subjected as a template for spray coating process. The different strategy was utilized for mass production of exfoliated MXene and all form of MXene synthesized were utilized for composite preparation. The composites are light in weight, which possess thickness range of 0.04–0.16 cm and density laid between 0.988–1.336 g cm^{-1}. In which MXPATPPy held lower density and uMXPAT exhibited lower thickness. The range of R_s is 1.6–160 000 Ω while MXPATPPy and MXPATPNPA showed higher and lower R_s, respectively; corresponding ρ was 256 000 Ω cm and 0.128 Ω cm, respectively. On the other hand, MXPATPNPA showed an excellent EC of 7.813 S cm^{-1}. Moreover, the composite had minimal thermal degradation till 175 °C. The thermal diffusivity range of the composites were 0.185–0.282 mm^2 s^{-1} whereas composites hold 0.384–0.687 W (m K)$^{-1}$, 1.889–2.247 J (g K)$^{-1}$ and 0.892–1.330 W s$^{1/2}$ m^{-2} K^{-1} range of thermal conductivity, heat capacity and thermal diffusivity, respectively. The uMXPAT had 0.282 mm^2 s^{-1} and 0.687 W (m K)$^{-1}$ of higher thermal diffusivity and thermal

conductivity, respectively. While MXPAT showed 2.247 J (g K)$^{-1}$ and 1.330 W s$^{1/2}$ m^{-2} K^{-1} of heat capacity and thermal effusivity, respectively. The MXPATPA exhibited maximum EMI shielding of 45.18 dB (9.31–12.4 GHz) with 33.26 dB g^{-1} cm^3, 236.45 dB g^{-1} cm^2 and 1.6 dB mm^{-1} of SSE, SSE/t and SE/t, respectively. The composites blocked almost 99.99% of incident radiation and maximum SE range of 45.18–39.33 dB while SSE, SSE/t and SE/t range were 27.99–40.49 dB g^{-1} cm^3, 236.45–721.25 dB g^{-1} cm^2 and 1.393–1.6 dB mm^{-1}, respectively. The composites possess excellent EMI shielding ability, flexibility and good thermal behaviors. Thus, composites can be utilized for both thermal and EMI shielding applications.

Conflicts of interest

The authors declare no conflict of interest.

Acknowledgements

References

1 Y. J. Yim, D. C. Chung and S. J. Park, EMI shielding effectiveness and mechanical properties of MWCNTs-reinforced biodegradable epoxy matrix composites, *Carbon Letters*, 2017, **22**, 36–41.

2 S. Engels, N. L. Schneider, N. Lefeldt, C. M. Hein, M. Zapka, A. Michalik, D. Elbers, A. Kittel, P. J. Hore and H. Mouritsen, Anthropogenic electromagnetic noise disrupts magnetic compass orientation in a migratory bird, *Nature*, 2014, **509**(7500), 353.

3 S. Pothupitiya Gamage, K. Yang, R. Braveenth, K. Raagulan, H. Kim, Y. Lee, C. M. Yang, J. Moon and K. Chai, MWCNT coated free-standing carbon fiber fabric for enhanced performance in EMI shielding with a higher absolute EMI SE, *Materials*, 2017, **10**(12), 1350.

4 A. Wdowiak, P. A. Mazurek, A. Wdowiak and I. Bojar, Effect of electromagnetic waves on human reproduction, *Ann. Agric. Environ. Med.*, 2017, **24**(1), 13–18.

5 A. Asghari, A. A. Khaki, A. Rajabzadeh and A. Khaki, A review on Electromagnetic fields (EMFs) and the reproductive system, *Electron. Physician*, 2016, **8**(7), 2655.

6 S. J. Genuis, Fielding a current idea: exploring the public health impact of electromagnetic radiation, *Public Health*, 2008, **122**(2), 113–124.

7 P. Vecchia, Exposure of humans to electromagnetic fields. Standards and regulations, *Ann. Istituto Super. Sanita*, 2007, **43**(3), 260.

8 F. Ozdemir and A. Kargi, Electromagnetic waves and human health, in *Electromagnetic Waves*, IntechOpen, 2011.

9 P. Russer, Electromagnetic Compatibility Engineering for Electronic Circuits and Devices, in *Proceedings of IEEE CALCON 2014, National Conference on Electrical, Electronics, and Computer Engineering*, Gallery 2 Technical Session T4 (EC), 2014.

10 J. Shapira, Electromagnetic Compatibility for System Engineers, *IETE Tech. Rev.*, 2011, **28**(1), 70–77.

11 W. T. Cao, F. F. Chen, Y. J. Zhu, Y. G. Zhang, Y. Y. Jiang, M. G. Ma and F. Chen, Binary strengthening and toughening of MXene/cellulose nanofiber composite paper with nacre-inspired structure and superior electromagnetic interference shielding properties, *ACS Nano*, 2018, **12**(5), 4583–4593.

12 R. Liu, M. Miao, Y. Li, J. Zhang, S. Cao and X. Feng, Ultrathin Biomimetic Polymeric Ti$_3$C$_2$T$_x$ MXene Composite Films for Electromagnetic Interference Shielding, *ACS Appl. Mater. Interfaces*, 2018, **10**(51), 44787–44795.

13 Q. W. Wang, H. B. Zhang, J. Liu, S. Zhao, X. Xie, L. Liu, R. Yang, N. Koratkar and Z. Z. Yu, Multifunctional and Water-Resistant MXene-Decorated Polyester Textiles with Outstanding Electromagnetic Interference Shielding and Joule Heating Performances, *Adv. Funct. Mater.*, 2019, **29**(7), 1806819.

14 F. Shahzad, M. Alhabeb, C. B. Hatter, B. Anasori, S. M. Hong, C. M. Koo and Y. Gogotsi, Electromagnetic interference shielding with 2D transition metal carbides (MXenes), *Science*, 2016, **353**(6304), 1137–1140.

15 S. K. Yee and M. Z. M. Jenu, Electromagnetic Shielding of Cement-Graphite Powder Between 100 to 2000 MHz, *ARPN J. Eng. Appl. Sci.*, 2015, 1–4.

16 R. Bian, G. He, W. Zhi, S. Xiang, T. Wang and D. Cai, Ultralight MXene-based aerogels with high electromagnetic interference shielding performance, *J. Mater. Chem. C*, 2019, **7**(3), 474–478.

17 L. W. Shacklette, N. F. Colaneri, V. G. Kulkarni and B. Wessling, EMI shielding of intrinsically conductive polymers, *J. Vinyl Addit. Technol.*, 1992, **14**(2), 118–122.

18 K. Raagulan, R. Braveenth, H. Jang, Y. Seon Lee, C. M. Yang, B. Mi Kim, J. Moon and K. Chai, Electromagnetic shielding by MXene-graphene-PVDF composite with hydrophobic, lightweight and flexible graphene coated fabric, *Materials*, 2018, **11**(10), 1803.

19 D. Jiang, V. Murugadoss, Y. Wang, J. Lin, T. Ding, Z. Wang, Q. Shao, C. Wang, H. Liu, N. Lu and R. Wei, Electromagnetic interference shielding polymers and nanocomposites-a review, *Polym. Rev.*, 2019, **59**(2), 280–337.

20 L. C. Jia, D. X. Yan, X. Jiang, H. Pang, J. F. Gao, P. G. Ren and Z. M. Li, Synergistic Effect of Graphite and Carbon Nanotubes on Improved Electromagnetic Interference Shielding Performance in Segregated Composites, *Ind. Eng. Chem. Res.*, 2018, **57**(35), 11929–11938.

21 T. T. Li, A. P. Chen, P. W. Hwang, Y. J. Pan, W. H. Hsing, C. W. Lou, Y. S. Chen and J. H. Lin, Synergistic effects of micro-/nano-fillers on conductive and electromagnetic shielding properties of polypropylene nanocomposites, *Mater. Manuf. Processes*, 2018, **33**(2), 149–155.

22 J. A. Pomposo, J. Rodríguez and H. Grande, Polypyrrole-based conducting hot melt adhesives for EMI shielding applications, *Synth. Met.*, 1999, **104**(2), 107–111.

23 M. K. Erdoğan, M. Karakişla and M. Saçak, Preparation, characterization and electromagnetic shielding

effectiveness of conductive polythiophene/poly(ethylene terephthalate)composite fibers, *J. Macromol. Sci., Part A: Pure Appl. Chem.*, 2012, **49**(6), 473–482.

24 J. Liu, H. B. Zhang, R. Sun, Y. Liu, Z. Liu, A. Zhou and Z. Z. Yu, Hydrophobic, flexible, and lightweight MXene foams for high-performance electromagnetic-interference shielding, *Adv. Mater.*, 2017, **29**(38), 1702367.

25 Z. Zhou, J. Liu, X. Zhang, D. Tian, Z. Zhan and C. Lu, Ultrathin MXene/Calcium Alginate Aerogel Film for High-Performance Electromagnetic Interference Shielding, *Adv. Mater. Interfaces*, 2019, **6**(6), 1802040.

26 X. Yang, S. Fan, Y. Li, Y. Guo, Y. Li, K. Ruan, S. Zhang, J. Zhang, J. Kong and J. Gu, Synchronously improved electromagnetic interference shielding and thermal conductivity for epoxy nanocomposites by constructing 3D copper nanowires/thermally annealed graphene aerogel framework, *Composites, Part A*, 2020, **128**, 105670.

27 Y. Zhang, L. Wang, J. Zhang, P. Song, Z. Xiao, C. Liang, H. Qiu, J. Kong and J. Gu, Fabrication and investigation on the ultra-thin and flexible $Ti_3C_2T_x$/co-doped polyaniline electromagnetic interference shielding composite films, *Compos. Sci. Technol.*, 2019, **183**, 107833.

28 A. Tanvir, P. Sobolčiak, A. Popelka, M. Mrlik, Z. Spitalsky, M. Micusik, J. Prokes and I. Krupa, Electrically conductive, transparent polymeric nanocomposites modified by 2D $Ti_3C_2T_x$ (MXene), *Polymers*, 2019, **11**(8), 1272.

29 K. J. Zhang, D. B. Lu, B. Da and Z. J. Ding, Coupling of Surface Plasmon Modes and Refractive Index Sensitivity of Hollow Silver Nanoprism, *Sci. Rep.*, 2018, **8**(1), 15993.

30 M. Alhabeb, K. Maleski, B. Anasori, P. Lelyukh, L. Clark, S. Sin and Y. Gogotsi, Guidelines for Synthesis and Processing of Two-Dimensional Titanium Carbide ($Ti_3C_2T_x$ MXene), *Chem. Mater.*, 2017, **29**(18), 7633–7644.

31 J. Luo, W. Zhang, H. Yuan, C. Jin, L. Zhang, H. Huang, C. Liang, Y. Xia, J. Zhang, Y. Gan and X. Tao, Pillared structure design of MXene with ultralarge interlayer spacing for high-performance lithium-ion capacitors, *ACS Nano*, 2017, **11**(3), 2459–2469.

32 J. Palisaitis, I. Persson, J. Halim, J. Rosen and P. O. Persson, On the structural stability of MXene and the role of transition metal adatoms, *Nanoscale*, 2018, **10**(23), 10850–10855.

33 R. Lotfi, M. Naguib, D. E. Yilmaz, J. Nanda and A. C. Van Duin, A comparative study on the oxidation of two-dimensional Ti_3C_2 MXene structures in different environments, *J. Mater. Chem. A*, 2018, **6**(26), 12733–12743.

34 N. Zhang, Y. Hong, S. Yazdanparast and M. A. Zaeem, Superior structural, elastic and electronic properties of 2D titanium nitride MXenes over carbide MXenes: a comprehensive first principles study, *2D Materials*, 2018, **5**(4), 045004.

35 Z. M. Sun, Progress in research and development on MAX phases: a family of layered ternary compounds, *Int. Mater. Rev.*, 2011, **56**(3), 143–166.

36 J. Stejskal and R. G. Gilbert, Polyaniline: Preparation of a conducting polymer (IUPAC technical report), *Pure Appl. Chem.*, 2002, **74**(5), 857–867.

37 G. Thenmozhi, P. Arockiasamy and R. J. Santhi, Isomers of poly aminophenol: chemical synthesis, characterization, and its corrosion protection aspect on mild steel in 1 M HCl, *Int. J. Electrochem.*, 2014, **2014**, 1–11.

38 A. Yussuf, M. Al-Saleh, S. Al-Enezi and G. Abraham, Synthesis and Characterization of Conductive Polypyrrole: The Influence of the Oxidants and Monomer on the Electrical, Thermal, and Morphological Properties, *Int. J. Polym. Sci.*, 2018, **2018**, 1–7.

39 Z. Wang, Y. Wang, D. Xu, E. S. W. Kong and Y. Zhang, Facile synthesis of dispersible spherical polythiophene nanoparticles by copper (II) catalyzed oxidative polymerization in aqueous medium, *Synth. Met.*, 2010, **160**(9–10), 921–926.

40 M. Nasrollahzadeh, M. Jahanshahi, M. Salehi, M. Behzad and H. Nasrollahzadeh, Synthesis and characterization of nanostructured polythiophene in aqueous medium by soft-template method, *J. Appl. Chem.*, 2013, **8**, 31–34.

41 A. Mockutè, *Synthesis and Characterization of New MAX Phase Alloys*, Doctoral dissertation, Linköping University Electronic Press, 2014.

42 Y. Tan, H. Luo, X. Zhou, S. Peng and H. Zhang, Dependences of microstructure on electromagnetic interference shielding properties of nano-layered Ti_3AlC_2 ceramics, *Sci. Rep.*, 2018, **8**(1), 7935.

43 A. Tariq, M. A. Iqbal, S. I. Ali, M. Z. Iqbal, D. Akinwande and S. Rizwan, Ti_3C_2-MXene/Bismuth Ferrite Nanohybrids for Efficient Degradation of Organic Dye and Colorless Pollutant, *ChemRxiv*, 2019, 1–33.

44 N. K. Chaudhari, H. Jin, B. Kim, D. San Baek, S. H. Joo and K. M. X. Lee, an emerging two-dimensional material for future energy conversion and storage applications, *J. Mater. Chem. A*, 2017, **5**(47), 24564–24579.

45 K. Raagulan, R. Braveenth, L. Ro Lee, J. Lee, B. M. Kim, J. J. Moon, S. B. Lee and K. Y. Chai, Fabrication of Flexible, Lightweight, Magnetic Mushroom Gills and Coral-Like MXene–Carbon Nanotube Nanocomposites for EMI Shielding Application, *Nanomaterials*, 2019, **9**(4), 519.

46 C. Di Franco, E. Beccari, T. Santini, G. Pisaneschi and G. Tecce, Colony shape as a genetic trait in the pattern-forming Bacillus mycoides, *BMC Microbiol.*, 2002, **2**(1), 33.

47 S. O. Mast, Structure, movement, locomotion, and stimulation in amoeba, *J. Morphol.*, 1926, **41**(2), 347–425.

48 P. Graat and M. A. Somers, Quantitative analysis of overlapping XPS peaks by spectrum reconstruction: determination of the thickness and composition of thin iron oxide films, *Surf. Interface Anal.*, 1998, **26**(11), 773–782.

49 T. W. Lee, S. E. Lee and Y. G. Jeong, Carbon nanotube/cellulose papers with high performance in electric heating and electromagnetic interference shielding, *Compos. Sci. Technol.*, 2016, **131**, 77–87.

50 A. Qian, S. E. Hyeon, J. Y. Seo and C. H. Chung, Capacitance changes associated with cation-transport in free-standing flexible $Ti_3C_2T_x$(TO,F,OH) MXene film electrodes, *Electrochim. Acta*, 2018, **266**, 86–93.

51 V. Datsyuk, M. Kalyva, K. Papagelis, J. Parthenios, D. Tasis, A. Siokou, I. Kallitsis and C. Galiotis, Chemical oxidation of multiwalled carbon nanotubes, *Carbon*, 2008, **46**, 833–840.

52 L. Wang, H. Zhang, B. Wang, C. Shen, C. Zhang, Q. Hu, A. Zhou and B. Liu, Synthesis and electrochemical performance of $Ti_3C_2T_x$ with hydrothermal process, *Electron. Mater. Lett.*, 2016, **12**, 702–710.

53 H. B. Zhang, Y. C. Zhou, Y. W. Bao and M. S. Li, Abnormal thermal shock behavior of Ti_3SiC_2 and Ti_3AlC_2, *J. Mater. Res.*, 2006, **21**, 2401–2407.

54 M. Han, X. Yin, H. Wu, Z. Hou, C. Song, X. Li, L. Zhang and L. Cheng, Ti_3C_2 MXenes with modified surface for high-performance electromagnetic absorption and shielding in the X-band, *ACS Appl. Mater. Interfaces*, 2016, **8**, 21011–21019.

55 A. Ivasyshyn, O. Ostash, T. Prikhna, V. Podhurska and T. Basyuk, Oxidation Resistance of Materials Based on Ti_3AlC_2 Nanolaminate at 600 °C in Air, *Nanoscale Res. Lett.*, 2016, **11**, 358.

56 T. A. Saleh, S. Agarwal and V. K. Gupta, Synthesis of $MWCNT/MnO_2$ and their application for simultaneous oxidation of arsenite and sorption of arsenate, *Appl. Catal., B*, 2011, **106**, 46–53.

57 P. Yan, R. Zhang, J. Jia, C. Wu, A. Zhou, J. Xu and X. Zhang, Enhanced supercapacitive performance of delaminated two-dimensional titanium carbide/carbon nanotube composites in alkaline electrolyte, *J. Power Sources*, 2015, **284**, 38–43.

58 V. Gupta and T. A. Saleh, Syntheses of carbon nanotube-metal oxides composites; adsorption and photo-degradation, in *Carbon Nanotubes-From Research to Applications*, InTech, Shanghai, China, 2011.

59 R. Leones, F. Sentanin, L. C. Rodrigues, I. M. Marrucho, J. M. S. S. Esperança, A. Pawlicka and M. M. Silva, Investigation of polymer electrolytes based on agar and ionic liquids, *Express Polym. Lett.*, 2012, **6**(12), 1007–1016.

60 H. Xu, J. Zhang, Y. Chen, H. Lu and J. Zhuang, Electrochemical polymerization of polyaniline doped with Cu^{2+} as the electrode material for electrochemical supercapacitors, *RSC Adv.*, 2014, **4**(11), 5547–5552.

61 Z. Zhou, X. Zhang, C. Lu, L. Lan and G. Yuan, Polyaniline-decorated cellulose aerogel nanocomposite with strong interfacial adhesion and enhanced photocatalytic activity, *RSC Adv.*, 2014, **4**(18), 8966–8972.

62 H. Duan, K. Zheng, L. Zhang and Y. Cui, Synthesis of poly (4-aminophenol) by horseradish peroxidase and the evaluation of its adsorptivity for silver ions, *J. Appl. Polym. Sci.*, 2014, **131**(12), 40367–40373.

63 K. Ahmed, F. Kanwal, S. Ramay, S. Atiq, R. Rehman, S. Ali and N. Alzayed, Synthesis and Characterization of $BaTiO_3$/ Polypyrrole Composites with Exceptional Dielectric Behaviour, *Polymers*, 2018, **10**(11), 1273.

64 S. Shrikrushna, J. A. Kher and M. V. Kulkarni, Influence of dodecylbenzene sulfonic acid doping on structural, morphological, electrical and optical properties on polypyrrole/3C-SiC nanocomposites, *J. Nanomed. Nanotechnol.*, 2015, **6**(5), 1.

65 J. Al Dream, C. Zequine, K. Siam, P. K. Kahol, S. R. Mishra and R. K. Gupta, Electrochemical Properties of Graphene Oxide Nanoribbons/Polypyrrole Nanocomposites, *C*, 2019, **5**(2), 18.

66 F. Zhang, Y. Shi, Z. Zhao, W. Song and Y. Cheng, Influence of semiconductor/insulator/semiconductor structure on the photo-catalytic activity of Fe_3O_4/SiO_2/polythiophene core/shell submicron composite, *Appl. Catal., B*, 2014, **150**, 472–478.

67 M. Sharif and B. Pourabas, Polythiophene–graphene oxide doped epoxy resin nanocomposites with enhanced electrical, mechanical and thermal properties, *RSC Adv.*, 2016, **6**(96), 93680–93693.

68 M. Hu, Z. Li, T. Hu, S. Zhu, C. Zhang and X. Wang, High-Capacitance Mechanism for Ti_3CT_x MXene by *in Situ* Electrochemical Raman Spectroscopy Investigation, *ACS Nano*, 2016, **10**(12), 11344–11350.

69 A. B. Rohom, P. U. Londhe, S. K. Mahapatra, S. K. Kulkarni and N. B. Chaure, Electropolymerization of polyaniline thin films, *High Perform. Polym.*, 2014, **26**(6), 641–646.

70 D. N. Huyen, N. T. Tung, N. D. Thien and L. H. Thanh, Effect of TiO_2 on the gas sensing features of TiO_2/PANi nanocomposites, *Sensors*, 2011, **11**(2), 1924–1931.

71 F. S. de Siqueira Oliveira, H. E. Giana and L. Silveira, Discrimination of selected species of pathogenic bacteria using near-infrared Raman spectroscopy and principal components analysis, *J. Biomed. Opt.*, 2012, **17**(10), 107004.

72 N. A. Zubair, N. A. Rahman, H. N. Lim, R. M. Zawawi and Y. Sulaiman, Electrochemical properties of PVA–GO/ PEDOT nanofibers prepared using electrospinning and electropolymerization techniques, *RSC Adv.*, 2016, **6**(21), 17720–17727.

73 K. Kumar and S. Murugesan, Synthesis, characterization and anti-bacterial activity of divalent transition metal complexes of hydrazine and trimesic acid, *J. Saudi Chem. Soc.*, 2018, **22**(1), 16–26.

74 C. Yong and Q. Renyuan, IR and Raman studies of polythiophene prepared by electrochemical polymerization, *Solid State Commun.*, 1985, **54**(3), 211–213.

75 X. Fan, Z. Yang and N. He, Hierarchical nanostructured polypyrrole/graphene composites as supercapacitor electrode, *RSC Adv.*, 2015, **5**(20), 15096–15102.

76 I. Rashid, N. H. Daraghmeh, M. M. Al Omari, B. Z. Chowdhry, S. A. Leharne, H. A. Hodali and A. A. Badwan, Magnesium silicate, in *Profiles of Drug Substances, Excipients and Related Methodology*, Academic Press, 2011, vol. 36, pp. 241–285.

77 M. Hafiezal, A. Khalina, Z. Zurina, M. Azaman and Z. Hanafee, Thermal and Flammability Characteristics of Blended Jatropha Bio-Epoxy as Matrix in Carbon Fiber–Reinforced Polymer, *J. Compos. Sci.*, 2019, **3**(1), 6.

78 X. Yang, C. Liang, T. Ma, Y. Guo, J. Kong, J. Gu, M. Chen and J. Zhu, A review on thermally conductive polymeric composites: classification, measurement, model and equations, mechanism and fabrication methods, *Adv. Compos. Hybrid Mater.*, 2018, **1**(2), 207–230.

79 R. Singh, G. Sandhu, R. Penna and I. Farina, Investigations for thermal and electrical conductivity of ABS-graphene blended prototypes, *Materials*, 2017, **10**(8), 881.

80 J. Szałapak, K. Kiełbasiński, J. Krzemiński, A. Młożniak, E. Zwierkowska, M. Jakubowska and R. Pawłowski, A

Method Of Calculating Thermal Diffusivity And Conductivity For Irregularly Shaped Specimens In Laser Flash Analysis, *Metrol. Meas. Syst.*, 2015, **22**(4), 521–530.

81 L. Vozár and W. Hohenauer, Flash method of measuring the thermal diffusivity. A review, *High. Temp.–High. Press.*, 2004, **36**(3), 253–264.

82 A. L. Cottrill, A. T. Liu, Y. Kunai, V. B. Koman, A. Kaplan, S. G. Mahajan, P. Liu, A. R. Toland and M. S. Strano, Ultra-high thermal effusivity materials for resonant ambient thermal energy harvesting, *Nat. Commun.*, 2018, **9**(1), 664.

83 H. Lei, C. Fu, Y. Zou, S. Guo and J. Huo, A thermal energy storage composite with sensing function and its thermal conductivity and thermal effusivity enhancement, *J. Mater. Chem. A*, 2019, **7**(12), 6720–6729.

84 H. U. Zaman, C. E. Shourov, A. Al Mahmood and N. E. A. Siddique, Conversion of wasted heat energy into electrical energy using TEG, in *2017, IEEE 7th Annual Computing and Communication Workshop and Conference (CCWC)*, IEEE., 2017, pp. 1–5.

85 T. Kyono, R. O. Suzuki and K. Ono, Conversion of unused heat energy to electricity by means of thermoelectric generation in condenser, *IEEE Trans. Energy Convers.*, 2003, **18**(2), 330–334.

86 R. Kang, Z. Zhang, L. Guo, J. Cui, Y. Chen, X. Hou, B. Wang, C. T. Lin, N. Jiang and J. Yu, Enhanced Thermal Conductivity of Epoxy Composites Filled with 2D Transition Metal Carbides (MXenes) with Ultralow Loading, *Sci. Rep.*, 2019, **9**(1), 9135.

87 Y. Cao, Q. Deng, Z. Liu, D. Shen, T. Wang, Q. Huang, S. Du, N. Jiang, C. T. Lin and J. Yu, Enhanced thermal properties of poly(vinylidene fluoride) composites with ultrathin nanosheets of MXene, *RSC Adv.*, 2017, **7**(33), 20494–20501.

88 S. Ningaraju and H. B. Ravikumar, Studies on electrical conductivity of PVA/graphite oxide nanocomposites: a free volume approach, *J. Polym. Res.*, 2017, **24**(1), 11.

89 T. J. Trivedi, K. S. Rao and A. Kumar, Facile preparation of agarose–chitosan hybrid materials and nanocomposite ionogels using an ionic liquid *via* dissolution, regeneration and sol–gel transition, *Green Chem.*, 2014, **16**(1), 320–330.

90 R. Liu and Z. Liu, Polythiophene: synthesis in aqueous medium and controllable morphology, *Chin. Sci. Bull.*, 2009, **54**(12), 2028–2032.

91 J. C. Thiéblemont, J. L. Gabelle and M. F. Planche, Polypyrrole overoxidation during its chemical synthesis, *Synth. Met.*, 1994, **66**(3), 243–247.

92 C. H. Du, Y. Y. Xu and B. K. Zhu, Plasticizer effect of dibutyl phthalate on the morphology and mechanical properties of hard elastic poly(vinylidene fluoride) fibers, *J. Appl. Polym. Sci.*, 2009, **114**(6), 3645–3651.

93 N. Ieda, K. Mantri, Y. Miyata, A. Ozaki, K. Komura and Y. Sugi, Esterification of long-chain acids and alcohols catalyzed by ferric chloride hexahydrate, *Ind. Eng. Chem. Res.*, 2008, **47**(22), 8631–8638.

94 M. Guillot, D. Ruhlmann and M. Buri, Use of glycerol as an agent to improve the self-dispersing properties of a mineral material to be added to an aqueous composition, *US Pat.*, 163147, Omya International AG and Coatex SAS, 2015.

95 J. Liu, H. B. Zhang, X. Xie, R. Yang, Z. Liu, Y. Liu and Z. Z. Yu, Multifunctional, superelastic, and lightweight MXene/polyimide aerogels, *Small*, 2018, **14**(45), 1802479.

96 M. Han, X. Yin, K. Hantanasirisakul, X. Li, A. Iqbal, C. B. Hatter, B. Anasori, C. M. Koo, T. Torita, Y. Soda and L. Zhang, Anisotropic MXene Aerogels with a Mechanically Tunable Ratio of Electromagnetic Wave Reflection to Absorption, *Adv. Opt. Mater.*, 2019, **7**(10), 1900267.

97 W. Xin, G. Q. Xi, W. T. Cao, C. Ma, T. Liu, M. G. Ma and J. Bian, Lightweight and flexible MXene/CNF/silver composite membranes with a brick-like structure and high-performance electromagnetic-interference shielding, *RSC Adv.*, 2019, **9**(51), 29636–29644.

98 X. Shui and D. D. L. Chung, Nickel filament polymer-matrix composites with low surface impedance and high electromagnetic interference shielding effectiveness, *J. Electron. Mater.*, 1997, **26**, 928–934.

99 W. Cao, C. Ma, S. Tan, M. Ma, P. Wan and F. Chen, Ultrathin and Flexible CNTs/MXene/Cellulose Nanofibrils Composite Paper for Electromagnetic Interference Shielding, *Nano-Micro Lett.*, 2019, **11**(1), 72.

100 L. Geng, P. Zhu, Y. Wei, R. Guo, C. Xiang, C. Cui and Y. Li, A facile approach for coating $Ti_3C_2T_x$ on cotton fabric for electromagnetic wave shielding, *Cellulose*, 2019, **26**(4), 2833–2847.

101 K. Raagulan, R. Braveenth, H. J. Jang, Y. S. Lee, C. M. Yang, B. M. Kim, J. J. Moon and K. Y. Chai, Fabrication of Nonwetting Flexible Free-Standing MXene-Carbon Fabric for Electromagnetic Shielding in S-Band Region, *Bull. Korean Chem. Soc.*, 2018, **39**(12), 1412–1419.